National Defense
Defence nationale

AD-A263 661

DRES

2

SUFFIELD REPORT

NO. 582

EXPERIMENTAL STUDY OF LOCATION AND
IDENTIFICATION OF FERROUS SPHEROIDS USING
A "SMART" TOTAL FIELD MAGNETOMETER

DTIC
S ELECTE
MAY 5 1993
C D

by

John E. McFee, Robert Ellingson and Yogadhish Das

93-09604

January 1993

DEFENCE RESEARCH ESTABLISHMENT SUFFIELD : RALSTON : ALBERTA

Canada

DEFENCE RESEARCH ESTABLISHMENT SUFFIELD
RALSTON, ALBERTA

SUFFIELD REPORT NO. 582

EXPERIMENTAL STUDY OF LOCATION AND IDENTIFICATION OF FERROUS SPHEROIDS USING A "SMART" TOTAL FIELD MAGNETOMETER

by

John E. McFee, Robert Ellingson and Yogadhish Das

DTIC QUALITY INSPECTED 5

Accesion For		
NTIS CRA&I	☑	
DTIC TAB	☐	
Unannounced	☐	
Justification		
By		
Distribution /		
Availability Codes		
Dist	Avail and / or Special	
A-1		

DRES-SR-582

ABSTRACT

A microprocessor-controlled magnetometer which accurately locates and identifies compact ferrous objects in real-time is described. The person-portable instrument consists of a cart-mounted cesium magnetometer, optical encoder, microcontroller, interface and laptop computer. The instrument guides the operator to collect simultaneous magnetic field and position data in a horizontal plane above an object. Custom algorithms estimate location and dipole moment and use the latter to classify the object. Data collection takes 6 - 13 minutes, location and moment estimation 5 seconds, classification 30 seconds. Experiments using two ferrous spheroids and studies using magnetic total field and vertical component magnetic maps generated by a mathematical computer model are described. Limits of error in estimation of location and dipole moment, error in classification, and relative effects of sources of error are quantified. The rms error for location vector components was 0.019 m - 0.045 m compared to the average precision of 0.003 m - 0.005 m. The average magnitude of the difference between estimated and theoretical dipole moment vectors as a percentage of the theoretical dipole moment was $24.5 \pm 11.4\%$ compared to precision of 0.51 - 8.21%. Pattern classification with a computer generated dipole moment design set is described. Deviation between experimental moment estimates and the computer model degraded performance but the misclassification rate for the two objects for which experimental measurements were made was 11.1%. If an experimental design set were used, analysis shows that the limiting misclassification error for the present experimental precision should be between 2 and 5%.

iii

RÉSUMÉ

On décrit un magnétomètre, piloté par un microprocesseur, qui permet de localiser et d'identifier rapidement en temps réel des objets ferreux compacts. L'appareil, qui peut être porté par une personne, est constitué d'un magnétomètre au césium, d'un codeur optique, d'un micro-contrôleur, d'une interface et d'un ordinateur portatif, le tout monté sur un chariot. L'appareil permet à l'utilisateur d'obtenir simultanément des données sur le champ magnétique et la position dans un plan horizontal au-dessus d'un objet. Des algorithmes élaborés sur mesure permettent d'estimer le moment dipolaire et sa position et d'utiliser ces données pour classer l'objet. Il faut de 6 à 13 minutes pour obtenir les données, 5 secondes pour estimer le moment et la position et 30 secondes pour classer l'objet. On décrit des expériences avec deux sphéroïdes ferreux, ainsi que des études effectuées avec des cartes du champ magnétique total et de la composante magnétique verticale, produites à l'aide d'un modèle mathématique sur ordinateur. On détermine l'importance des limites d'erreur sur l'estimation du moment dipolaire et de sa position, de l'erreur de classement, ainsi que des effets relatifs des sources d'erreur. L'erreur quadratique moyenne sur les composantes du vecteur de position était de 0,019 m - 0,045 m, en comparaison avec la précision moyenne de 0,003 m - 0,005 m. La grandeur moyenne de l'écart entre la valeur estimée et la valeur théorique des vecteurs du moment dipolaire, exprimée en pourcentage du moment dipolaire théorique, était de 24,5 $\pm$ 11,4 %, en comparaison avec la précision qui était de 0,51 - 8,21 %. On décrit le classement des résultats réalisés à l'aide d'un ensemble de référence de moments dipolaires créé par ordinateur. L'écart entre les moments estimés expérimentalement et les valeurs obtenues par modélisation informatique diminuait le rendement de l'appareil; néanmoins, le taux de classement incorrect pour les deux sphéroïdes ayant fait l'objet des mesures expérimentales était de 11,1 %. L'analyse révèle que, pour un ensemble de référence expérimental, la limite d'erreur de classement devrait être comprise entre 2 et 5 % pour la présente précision expérimentale.

iii

RÉSUMÉ

Executive Summary

Magnetometers have been used to detect ferrous objects in a wide range of military and civilian applications since the 1930's. Magnetometers produce a signal which is indicative of magnetic field strength, but do not explicitly provide the accurate location or identity of a detected object. In a number of applications, particularly the clearance of old artillery ranges and mine detection, such an ability would be very desirable. Several research groups in several countries have developed data logging magnetometers with limited location and identification capability for large scale surveys of magnetic anomalies. However, all the instruments must transfer data to a computer which analyses the data off-line. They can localize a compact ferrous object to within a few times its depth of burial and they can classify an object in terms of its rough size. None of them can explicitly determine the location to within a fraction of the depth and explicitly determine the identity of the detected object in real-time.

This report presents an improved "smart" magnetometer. Based on an earlier prototype produced by this laboratory, the new version is the first magnetometer having the ability to explicitly and accurately locate and identify compact ferrous objects in real-time. The instrument, which is person-portable but could be modified for vehicle mounting, consists of a cesium vapour magnetometer mounted on a cart with a wheel-mounted optical encoder, a microcontroller, interface and a laptop computer. The instrument guides the operator in the collection of simultaneous magnetic field and position data in a horizontal plane above an object. Location is estimated by applying a custom location algorithm to the data and identity is established by a custom pattern classification using a byproduct of the location algorithm, the dipole moment, as a feature vector. The instrument is more robust and user friendly than the earlier prototype and its accuracy in estimating location and dipole moment vectors has been improved. Design sets of dipole moments (used for comparison in the pattern classifier) can now be updated in the field. The user interface uses a lap-top computer to communicate with the magnetometer's microcontroller and is much less cryptic than the previous version's keypad and four digit display. Magnetic field data and design sets can be transferred between the computer and the microcontroller. With the present instrument, as few as 6 minutes are required to collect the data, location and dipole moment estimation requires 5 seconds and classification requires 30 seconds.

To quantify the performance of the instrument, a detailed study was recently completed to determine the error in estimating the location and dipole moment of ferrous spheroids. Spheroids were chosen because they can be similar in shape and size to unexploded ordnance and have magnetic fields that well approximate those of unexploded ordnance. Also, a mathematical model for the static magnetic field of a spheroid induced by a homogeneous magnetic field exists which can be used both to generate design sets and to aid in analysing estimation errors. Experiments were performed using two different ferrous spheroids.

The precision in estimating location varied from 0.12 to 1.35% of the depth for a fixed

DRES-SR-582

object and orientation at a given depth. There was a slight variation in location estimate with object type and/or orientation which increased the location uncertainty to 1.67 to 1.90% of the depth. The precision in estimating the dipole moment varied from 0.51 to 8.21 % of the dipole moment magnitude. There was a slight increase in uncertainty as depth decreased, but the precision was not closely correlated with peak magnetic field.

All three components of the location estimate had a depth dependent bias which was larger than can be accounted for by the precision of the estimation. Errors in the vertical component were generally larger than those for the horizontal components. The root mean square (RMS) error over all depths was 0.020 m and 0.019 m for the two horizontal components of location and 0.045 m for the vertical component. By comparison, the average precision for a fixed object and orientation was 0.005 m and 0.003 m for the two horizontal components and 0.004 m for the vertical component.

There was a deviation between theoretical values and experimental estimates of the dipole moment that was greater than the uncertainties in the estimates. The unweighted average difference between estimated and theoretical dipole moment components as a percentage of the theoretical dipole moment was $4.8 \pm 7.6\%$ and $-3.3 \pm 15.5\%$ for the two horizontal components of the dipole moment, $-10.8 \pm 17.5\%$ for the vertical component and $24.5 \pm 11.4\%$ for the magnitude of the vector difference. There was no clear trend with object type, orientation or depth.

Following quantification of the error in the estimation of location and dipole moment, sources of error and their relative effects were analysed. By applying the location algorithm to magnetic total field and vertical component data generated by mathematical computer model, the relative contribution of the various error sources could be estimated. It was argued that a substantial fraction of the uncertainty (precision) in dipole location and moment vector estimates was due to positional uncertainty in the experiments. It was also demonstrated, however, that positional error in these experiments had little influence on the overall location and moment vector estimation and that remnant magnetization in the spheroids must be small compared to the induced magnetization. It was shown that the finite volume of the sensor head was not a significant source of error for the geometry of these experiments. A variation of error with depth and object orientation was noticed for the computer generated data. This suggested that the main contributor to the error was estimation of the position of the field extrema and the use of total field in place of vertical component magnetic data. Ultimately, it was estimated that the error due to the total field approximation varied from 14 to 18% of the moment magnitude and that the error due to estimation of extrema positions and higher order moments varied from 0 to 8% of the moment magnitude.

The analysis of error in the computer generated total magnetic field data also allowed limits to be set on the misclassification rate that can ultimately be attained. The moment estimates for a given object and orientation were found to vary by between 2 and 4% of

the moment magnitude as the depth varied. If the estimated moments were used in the design set, this suggests that the limiting misclassification error would be between roughly 1.4 and 2.4% if the experimental (mainly positional) error were substantially less than the algorithmic and approximation errors. For the present experimental precision ($4.1 \pm 3.0\%$), the misclassification error should be roughly between 2 and 5% (assuming quadrature error summation) if the design set were experimentally obtained.

Pattern classification was performed with a computer generate dipole moment design set consisting of 8 objects including the 2 used in these experiments. The gross misclassification rate was 10.3% for the class number 4 spheroid and 100% for class number 6. Closer examination revealed that class 6 was always classified as class number 3, which is a similarly shaped spheroid. This is likely due to the deviation between the moment estimates for the experimental spheroid and the computer model. The repeatability of classification, that is, the percentage of cases in which an object is classified as the same class, is a better measure of classifier performance. The repeatability of classification was 91.7%. If we consider only the two objects for which experimental measurements were made, we see that only 4/36 cases (11.1%) were classified incorrectly.

The overall performance of the smart magnetometer is very encouraging. The report closes with a discussion of future work that must be done to improve the instrument and to make it successful as a practical locator and identifier for buried ferrous ordnance.

DRES-SR-582

DRES-SR-582

ACKNOWLEDGEMENT

x

Table of Contents

List of Figures

List of Tables

DRES-SR-582

1. Introduction

Magnetometers have been used to detect ferrous objects in a wide range of applications since the 1930's. Magnetometers produce a signal which is indicative of magnetic field strength, but do not explicitly provide the accurate location or identity of a detected object. In a number of applications, particularly the clearance of old artillery ranges and mine detection, such an ability would be very desirable. Several research groups have addressed the problem of large scale surveys to detect magnetic anomalies. A vehicle-towed detector array, STOLS, has been developed by Geo-Centers Inc., Newton Falls, MA, USA, for the US Navy [1] to locate magnetic anomalies over areas of several thousand square meters. The device consists of a set of commercially available cesium vapour magnetometers and a microwave triangulation position measurement system connected to a data collection system. Data is processed off-line to produce field intensity maps which can be interpreted to roughly locate magnetic objects. Further, compact magnetic objects such as artillery shells can be located more accurately and roughly grouped in size, based on dipole strength, using a fairly slow iterative nonlinear least squares fit dipole locator algorithm originally developed by our laboratory [2]. Another large area magnetic field mapping instrument, the TM-3, has been developed by the University of New England, Australia [3]. This hand-held instrument, which is based on a single cesium vapour sensor, uses a data logger to collect a magnetic field map. Data is transferred to a PC which produces images of the magnetic field in a plane and allows rough localization and identification of anomalies by visual inspection of the shape of the magnetic field. Institut Dr. Forster, Reutlingen, Germany, manufactures a hand-held fluxgate gradiometer, the FEREX CAST 4.021.06, which is intended for smaller areas. It can log data while scanning an area, then transfer the data to a PC for off-line analysis [4]. A similar data logging magnetometer with a PC analysis package, called CAMAD, was announced some time ago by Aprotec Ltd., Manchester, UK [5], but nothing has been heard of it since the initial announcement. All these instruments must transfer data to a computer which analyses the data off-line. They can localize a compact ferrous object to within a few times its depth of burial (the exception being STOLS using the DRES iterative location algorithm) and can classify an object in terms of its rough size. None of them can explicitly determine the location to within a fraction of the depth and explicitly determine the identity of the detected object in real-time.

In [6], a real-time method to explicitly estimate the location and determine the identity of a compact ferrous object was presented. It was based on sampling the magnetic field

of the object in a horizontal plane, storing simultaneous position and magnetic field data, and then using a noniterative algorithm to determine the location and components of the dipole moment associated with the object. A byproduct of the location algorithm was an estimate of the dipole moment which was used by a DRES continuous parameter (CP) pattern classifier to identify the object. A prototype microprocessor-controlled cesium vapour "smart" magnetometer was described which collected simultaneous magnetic and position data and then used these algorithms to locate and identify ferrous spheres and spheroids. A few preliminary results were also reported. This was the first magnetometer with the ability to explicitly locate and identify compact ferrous objects and the first total field magnetometer with explicit object location estimation in a self-contained instrument.

This report presents an improved "smart" magnetometer. The new version is the first magnetometer having the ability to explicitly and accurately locate and identify compact ferrous objects in real-time. The instrument, which is person-portable, consists of a cesium vapour magnetometer mounted on a cart with a wheel-mounted optical encoder, a microcontroller, interface and a laptop computer. The instrument guides the operator in the collection of simultaneous magnetic field and position data in a horizontal plane above an object. Location is estimated as before by applying the DRES noniterative location algorithm to the data and identity is established by pattern classification using the dipole moment as a feature vector. The instrument is now more robust and user friendly than the earlier prototype and its accuracy in estimating location and dipole moment vectors has been improved. Design sets of dipole moments (used for comparison in the pattern classifier) can now be updated in the field. The user interface uses a lap-top computer to commmunicate with the magnetometer's microcontroller and is much less cryptic than the previous version's keypad and four digit display. Magnetic field data and design sets can be transferred between the computer and the microcontroller.

To quantify the performance of the instrument, a detailed study was recently completed to determine the error in estimating the location and dipole moment of ferrous spheroids. Spheroids were chosen because they can be similar in shape and size to unexploded ordnance and have magnetic fields that well approximate those of unexploded ordnance [7], [8]. Also, a mathematical model for the static magnetic field of a spheroid induced by a homogeneous magnetic field exists [8] which can be used both to generate design sets and to aid in analysing estimation errors. The present study has, in fact, identified several sources of error in an attempt to learn if and how they might be ameliorated.

Chapter 2 provides the necessary theoretical framework regarding magnetic field measurements, the location and moment estimation algorithm and the pattern classifier. Also the mathematical model for the magnetic field and dipole moment induced in a ferrous spheroid by a uniform magnetostatic field is also developed. The model is needed to generate design sets for the classifier as well as to analyse the performance of the location algorithm. Chapter 3 describes the magnetometer, the experimental layout, the data collection procedure and the initial calibration of the instrument. Chapter 4 presents the results of applying the location estimation algorithm to a large number of magnetic field maps of different objects, orientations and depths. In Chapter 5, the errors associated with the

location algorithm are analysed. This is facilitated by comparison with location estimation results based on total magnetic field maps and vertical component magnetic field maps generated by computer using the mathematical model. Performance of the pattern classifier is discussed in Chapter 6. Chapter 7 summarizes the performance of the instrument and discusses possible improvements to the instrument and procedures and further studies that should be done.

2. Theory

2.1 Magnetic Field Measurement

The spatial extent of the measureable magnetic fields associated with most compact objects of interest is generally less than a few hundred meters and the time taken to measure such fields is less than a few minutes. Fortunately, the earth's field is constant over such distances (magnetic induction gradient $\sim$ 10 nT/km) and does not change significantly during this time. In spite of occasional field nonuniformities arising from local magnetic phenomena, one can in practice usually assume that the ambient field is constant. A detailed description of the spatial and temporal variation of the earth's magnetic field and the field due to common terrestrial sources may be found in [9].

There are two types of magnetometers - vector sensors and total field sensors. The latter includes self-oscillating optically pumped cesium vapour magnetometers, such as the one used in the present work. Total field magnetometers measure the magnitude of the field but not its direction. Their chief advantage over vector sensors is that the former are insensitive to small changes in the orientation of the sensor. Principles of operation of cesium vapour magnetometers and low noise measurement techniques may be found in [9].

We will now discuss the signal measured by a total field magnetometer. The secondary field (field due to the object) in a cartesian coordinate system is denoted by $\vec{B} = (B_1, B_2, B_3)^T$, where the superscript T denotes the transpose. If the primary (ambient, i.e., earth's) field is $\vec{B}_0 = (B_{01}, B_{02}, B_{03})^T$, then a total field magnetometer would measure

$$B_t = \left\| \vec{B}_0 + \vec{B} \right\| = \left(B_0^2 + B^2 + 2\vec{B}_0 \cdot \vec{B} \right)^{1/2} . \tag{2.1}$$

Generally $B_0 \gg B$ and a Taylor expansion can be performed to obtain

$$B_t \approx B_0 + \hat{\gamma} \cdot \vec{B} + \frac{1}{2B_0} \left[B^2 - \left(\hat{\gamma} \cdot \vec{B} \right)^2 \right] - \frac{1}{2B_0^2} \left[\hat{\gamma} \cdot \vec{B} \right] \left[B^2 - \left(\hat{\gamma} \cdot \vec{B} \right)^2 \right] + \cdots \tag{2.2}$$

where

$$\hat{\gamma} = B_0^{-1} \vec{B}_0 . \tag{2.3}$$

To first order, a total field magnetometer measures the magnitude of the earth's field plus the projection of the magnitude of the object's field along the direction of the earth's field vector.

2.2 Estimation of Dipole Location and Moment

A space-fixed cartesian coordinate system with arbitrary origin is assumed (Fig. 2.1). Assume also a cartesian coordinate system centered at the dipole location (called the "dipole system"). Vector and tensor components in the space-fixed coordinate system are denoted by upper case symbols and those in the dipole system are denoted by lower case symbols. The system is oriented such that $\vec{m} = (m_1, 0, m_3)^T$, i.e., $m_2 = 0$ and the x_3 axis is parallel with the X_3 axis. The x_2 axis makes an angle α with the X_2 axis. Field measurements are
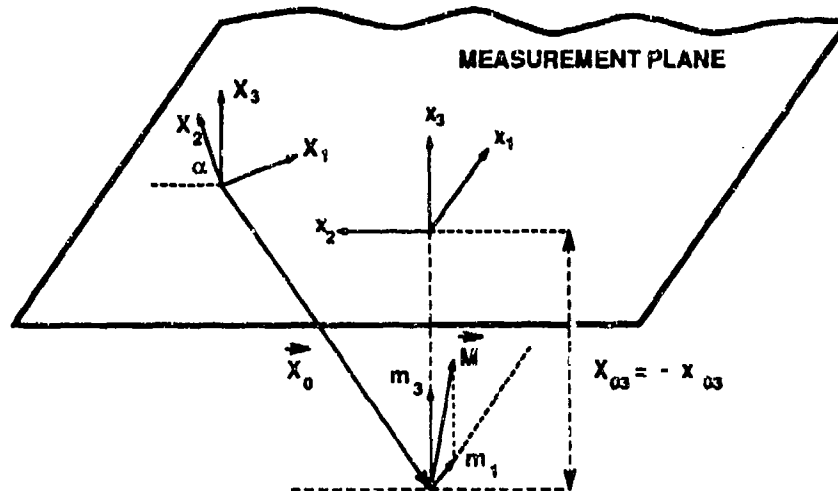
Figure 2.1

Geometry for magnetostatic dipole location.

made in the $x_3 = x_{03}$ plane. The measurement plane is chosen to be at $X_3 = 0$, without loss of generality, and $X_{03} = -x_{03}$ is referred to as the "depth" of the dipole. The measurement plane is normally horizontal and the x_3 axis is normally vertical. This is the geometry used in the experiments of this report and is similar to that found in most practical unexploded ordnance detection applications.

Various analytical and numerical methods have been derived to estimate the six independent dipole parameters (the three components of the location, $\vec{X}_0$, and moment, $\vec{M}$) from measurements of the dipole field or gradient [6]. The method used in this study is an algorithm developed at this laboratory which we have dubbed the extremum method. It has the advantage that it is noniterative, which makes it robust and quick. Most importantly, it

is the only noniterative algorithm for a generally oriented dipole which can use input data from a total field magnetometer. The algorithm is outlined below and is described in detail in [10].

If both a maximum and a minimum of a field quantity can be found in the plane of measurement, six independent pieces of information are available and the dipole parameters can in principle be determined. B_3 has more than one extremum and hence is a candidate for such a method. B_3 is not itself a rotationally invariant quantity. However, if the angle between the normal to the measurement plane and earth's field direction is $< \sim 15-20°$ (e.g., high to mid-latitudes), the 3-component of the secondary field is reasonably approximated by $(B_t - B_0)$ (Equation 2.2) and hence B_3 can be measured by a total field magnetometer which is insensitive to orientation. Note that the angle in question at our laboratory site is 17°.

It can be shown [10] that the positions (x_{1j}^e, x_{2j}^e) of the extrema of B_3 in the measurement plane are given by

$$x_{1j}^e = f_j(\beta)x_{03} \quad ; \quad x_{2j}^e = 0 \quad j = 1, 2, 3 \tag{2.4}$$

where f_j are monotonic analytic functions of $\beta = m_1/m_3$ whose ranges are $2 \leq f_1 \leq \infty$, $0 \leq f_2 \leq 1/2$ and $-2 \leq f_3 \leq -1/2$. The positions of the extrema lie in the plane along a straight line which coincides with the x_2 axis. (An exception is the case of a vertical dipole for which choice of x_2 axis is arbitrary. A maximum exists immediately above the dipole and a continuous ring of minima is centered on the maximum.) Thus, the angle α which relates the orientation of the dipole coordinate system to the space-fixed system is immediately known once the positions of the extrema are found. It turns out that $j = 2$ corresponds to a field maximum B_3^{max}, while $j = 3$ is a field minimum B_3^{min}, and $j = 1$ is a saddle point. The field values at the maximum or minimum are given by

$$B_3 = \frac{\mu_0}{4\pi} m x_{03}^{-3} \left(1 + \beta^2\right)^{-1/2} \left(1 + f_j^2\right)^{-3/2} \left[-1 + 3\left(1 + f_j^2\right)^{-1} \left(1 + \beta f_j\right)\right] \tag{2.5}$$

where $m = \sqrt{\vec{m}^T \vec{m}}$ and $j = 2$ (maximum) or 3 (minimum).

The ratio of the field minimum to the field maximum is a monotonic function of β which can be inverted by approximating the function for intervals of β by polynomials of the form

$$\beta = \sum_{k=0}^{n} a_{jk} \left(B_3^{min}/B_3^{max}\right)^k \tag{2.6}$$

where a_{jk} are the fitted coefficients for the jth interval of β. Three intervals with $3 \leq n \leq 6$ for each interval have given very accurate approximations to the function. The corresponding coefficients are given in [10].

The algorithm, then, is simple to implement. First the space-fixed coordinates of the position in the measurement plane of the maximum and minimum (X_{1j}^e, X_{2j}^e) are found and α is estimated. The differences in x_1 coordinates between the maximum and minimum are obtained by a simple rotation transformation using α. Next, β is deduced from the measured ratio of field minimum to maximum by Eq. 2.6 and is used to estimate f_2, f_3.

Estimates of f_2, f_3 and the differences in x_1 coordinates of maximum and minimum are inserted in Eq.2.4 to estimate X_{03}. The x_1 coordinates of the maximum and minimum are next calculated using Eq.2.4 and are used to find X_{01}, X_{02} from,

$$X_{01} = X_{1j}^c - x_{1j}^c \cos \alpha \quad ; \quad X_{02} = X_{2j}^c - x_{1j}^c \sin \alpha \qquad (2.7)$$

where $j = 2, 3$. The position $\vec{X}_0$ is now known and since β, α are known, the direction of $\vec{M}$ is completely specified. Finally, m, the magnitude of $\vec{M}$, is obtained from Eq.2.5.

Small modifications to the algorithm as described are necessary for the case of a vertical dipole, and some heuristics are used to handle minima that are too small to be observed [10].

2.3   Identification of a Spheroid From Its Dipole Moment

The previous algorithm can estimate the location and moment of the dipole associated with a compact ferrous object. However, it is the location and identity of the compact ferrous object that is required. Six parameters uniquely define a dipole source, but with the exception of the sphere, more than six parameters are needed to specify the compact object. This means that if field measurements are made at sufficient distance from a source so that higher order multipoles are negligible with respect to the dipole, one cannot in general distinguish between two compact orientable bodies. Information is necessary from higher order multipoles if the problem is to be have a unique inverse. Estimation of these multipoles is difficult, usually relying on fitting the field to a source model and solution is dependent on the shape of object.

Fortunately in practical applications there are usually a small number of object shapes and sizes applicable to a particular problem. If the dipole field associated with each object of the set is sufficiently different from that of the other objects, identity can be reliably determined from the dipole field. We will now outline the method that is used by the smart magnetometer to identify compact ferrous objects based on their magnetic dipole moments. It employs a novel pattern classification technique which is discussed more fully in [11].

It is assumed that we have determined the location and dipole moment components of the object relative to a space-fixed cartesian coordinate system by the method described in Section 2.2 and that the dipole location is at or near the geometric center of the object. The latter turns out to be a reasonable assumption (see discussion of the sources of dipole parameter estimation errors in Section 5.1). The plan is to use a pattern classification approach by which an object under scrutiny is identified by comparing a vector composed of features ("test vector") with feature vectors from a set of known objects ("design set"). The feature vector chosen will be the dipole moment vector.

The space-fixed components of the dipole moment induced in a homogeneous, permeable, axially symmetric, compact object by a uniform, static external magnetic field will vary with the orientation of the object. Since two angles define the orientation, the locus

of all possible dipole moments for such an object is actually a two dimensional surface in a three dimensional space. (The dipole moment is usually independent of the magnetic permeability of a ferrous object in the earth's field and so only one surface exists for each unique object shape and size.) For a spheroid, which also has fore-aft symmetry, unique values of the space-fixed magnetic dipole moment $\vec{M}$ occur only for the following range of the two continuous orientation parameters (θ, ϕ) $(\theta = \phi = 0)$, $(0 < \theta < \pi/2$ when $0 \le \phi < 2\pi)$ and $(\theta = \pi/2$ when $0 \le \phi < \pi)$.

Assume that a design set of dipole moments, $\vec{M}_{j,k}$, have been measured at discrete intervals (θ_j, ϕ_k) over the range of angles for which unique values of $\vec{M}$ occur. Consider the region of the dipole moment surface corresponding to class i for which $\theta_j \le \theta \le \theta_{j+1}$ and $\phi_k \le \phi \le \phi_{k+1}$. This region of the surface may be approximated by two triangles. One triangle passes through points $\vec{M}_{j,k}$; $\vec{M}_{j+1,k}$; $\vec{M}_{j,k+1}$ (index i is suppressed) and is bounded by $\vec{u}_{j,k}$, $\vec{v}_{j,k}$ and $\vec{u}_{j,k} - \vec{v}_{j,k}$, where

$$\vec{u}_{j,k} = \vec{M}_{j,k+1} - \vec{M}_{j,k} \quad , \quad \vec{v}_{j,k} = \vec{M}_{j+1,k} - \vec{M}_{j,k}. \tag{2.8}$$

The other triangle passes through points $\vec{M}_{j+1,k}$; $\vec{M}_{j+1,k+1}$; $\vec{M}_{j,k+1}$ and is bounded by $\vec{u}'_{j,k}$. $\vec{v}'_{j,k}$ and $\vec{u}'_{j,k} - \vec{v}'_{j,k}$, where

$$\vec{u}'_{j,k} = \vec{M}_{j+1,k} - \vec{M}_{j+1,k+1} \quad , \quad \vec{v}'_{j,k} = \vec{M}_{j,k+1} - \vec{M}_{j+1,k+1}. \tag{2.9}$$

If $\vec{x}$ is a test vector (suppressing subscripts j, k where unambiguous to do so), then

$$\vec{y}_{j,k} = \vec{x} - \vec{M}_{j,k} . \tag{2.10}$$

If $\vec{y}^{(s)}$ is he projection of $\vec{y}$ onto the unprimed triangle, a Gram-Schmidt construction gives

$$\vec{y}^{(s)} = p_{i,j,k}\vec{u} + q_{i,j,k}\vec{v} \tag{2.11}$$

where $p_{i,j,k}, q_{i,j,k}$ are scalars given by

$$q_{i,j,k} = \frac{\left(\vec{y}^T\vec{v}\right)\left(\vec{u}^T\vec{u}\right) - \left(\vec{y}^T\vec{u}\right)\left(\vec{u}^T\vec{v}\right)}{\left(\vec{v}^T\vec{v}\right)\left(\vec{u}^T\vec{u}\right) - \left(\vec{u}^T\vec{v}\right)^2} \quad , \quad p_{i,j,k} = \frac{\left(\vec{y}^T\vec{u}\right) - q\left(\vec{u}^T\vec{v}\right)}{\left(\vec{u}^T\vec{u}\right)}. \tag{2.12}$$

If $\vec{x}$ is a sample from the class i corresponding to the region of the dipole moment surface bounded by $\vec{u}, \vec{v}, \vec{u} - \vec{v}$, then estimates, $\hat{\theta}$ and $\hat{\phi}$, of the continuous parameters associated with $\vec{x}$ may be obtained from

$$\hat{\theta} = \theta_j + q_{i,j,k}\left(\theta_{j+1} - \theta_j\right) , \tag{2.13}$$

$$\hat{\phi} = \phi_k + p_{i,j,k}\left(\phi_{k+1} - \phi_k\right). \tag{2.14}$$

The minimum distance, $d_{i,j,k}$, from the test vector to the triangle is given by

$$\vec{d} = \vec{y} - \vec{y}^{(s)} \quad ; \quad d_{i,j,k} = \left(\vec{d}^T \vec{d} \right)^{1/2} . \tag{2.15}$$

The previous equations give the minimum distance to the triangle if $\vec{y}^{(s)}$ lies within the boundaries of the triangle. This is true provided $p_{i,j,k} \geq 0$, $q_{i,j,k} \geq 0$ and $0 \leq p_{i,j,k} + q_{i,j,k} \leq 1$. If these conditions are not satisfied, then $d_{i,j,k}$ is replaced by the minimum distance from the test vector to the line segments which bound the triangle.

A similar process is applied to the primed triangle, yielding a minimum distance $d'_{i,j,k}$. The minimum distance, d_i, from the test vector to the class i dipole moment surface is then approximated by

$$d_i = \min_{j,k} \left\{ d_{i,j,k}, d'_{i,j,k} \right\} . \tag{2.16}$$

The dipole moment surface for $\theta = 0$ is independent of ϕ. In this case, the manifold between $\theta_l = 0$, θ_{l+1}, ϕ_k and ϕ_{k+1} is approximated by a single triangle connecting $\vec{M}_l$, $\vec{M}_{l+1,k}$, $\vec{M}_{l+1,k+}$.

This classification method has been tested on a design set consisting of noise-free magnetic moments for six different spheroids, typical of the size and shape of a wide variety of artillery shells ($0.01 \leq a \leq 0.09$ m, $2.5 \leq e \leq 3.75$, where a, e are defined in Section 2.4). These were computer generated at $15°$ increments of the orientation angles θ, ϕ. Test vectors were computer generated at $5°$ increments with additive Gaussian noise of different levels. The probability of misclassification was about 1% for noiseless test vectors, 3% for moments with noise which was 5% of the moment component value for each component, and 7% for moments with 10% noise [11].

The identification method has been presented for a compact axially symmetric object but can be generalized to a compact body of arbitrary shape [11].

2.4   Multipole Expansion of the Magnetic Field of a Spheroid

In this Section, we present a mathematical model for the magnetic field induced in a homogeneous spheroid of arbitrary orientation by a uniform magnetostatic field. The model can be used both to develop a design set for use by the magnetometer's pattern classifier (see previous Section) and to provide controlled magnetic field data for analysis of the location estimation algorithm error. The model has been shown to provide magnetic fields that are a good approximation to those of real spheroids and some unexploded ordnance in the earth's field [7], [8]. A brief outline of the model is given below. A detailed derivation may be found in [9].

It is assumed that a homogeneous uniformly permeable spheroid, with magnetic permeability $\mu_{r1}\mu_0$ and no permanent magnetization, sits in a homogeneous surrounding medium

with permeability $\mu_{r2}\mu_0$, where μ_0 is the permeability of free space (Fig. 2.2). There
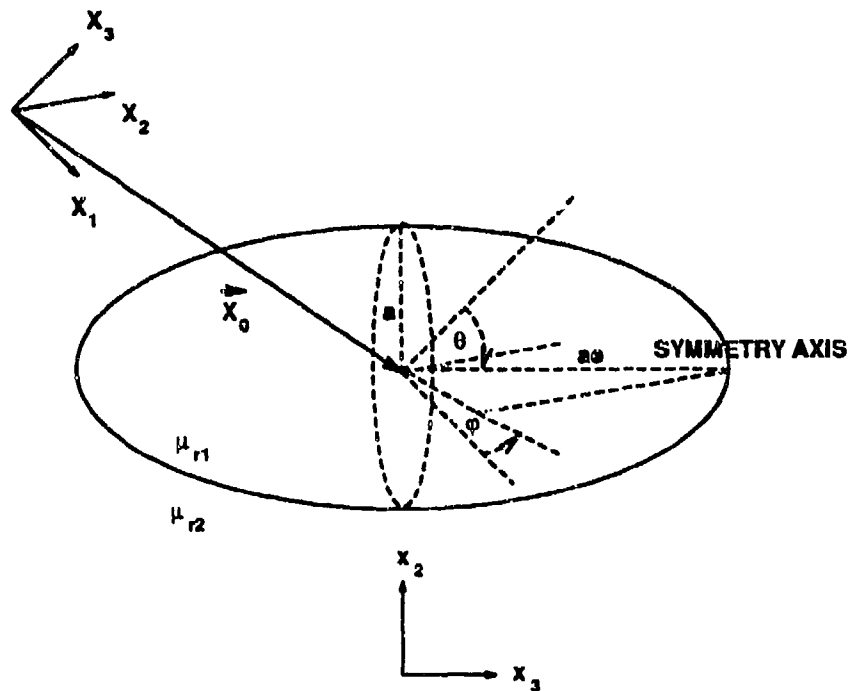
Figure 2.2

Geometry for calculation of the magnetic field of a spheroid.

exists a uniform parallel external magnetostatic field. A body-fixed cartesian coordinate system whose 3-axis coincides with the symmetry axis of the spheroid, has an origin at the geometric center of the spheroid. There is also a space-fixed coordinate system to which measurements are referenced. Without loss of generality, the space-fixed system is chosen so that the primary magnetic field, $\vec{B}_0$, has no 2-component, i.e., $\vec{B}_0 = (B_{01}, 0, B_{03})^T$. The spheroid center is located at $\vec{X}_0 = (X_{01}, X_{02}, X_{03})^T$ in this system. Vectors are indicated by lower case letters in the body-fixed system and upper case letters in the space-fixed system. The angle between the spheroid symmetry axis and the X_3 axis is θ. The angle between the projection of the symmetry axis on the horizontal plane and the X_1 axis is ϕ. It can be shown [12] that the induced field, and hence the magnetization, inside the spheroid is uniform and parallel. By carrying out a multipole expansion of the static field, and with the assumptions of uniform parallel internal magnetization, it may be shown that the secondary induced magnetic induction measured at a point $\vec{r} = (x_1, x_2, x_3)$ in free space, complete to fourth order, is given by [9]

$$\vec{b} = \vec{b^{(2)}} + \vec{b^{(8)}} \tag{2.17}$$

where $b^{(2)}$ is a dipole field term and $b^{(8)}$ is an octupole field term. The two field terms may

be expressed in component notation using summation convention as

$$b_\alpha^{(2)} = \frac{\mu_0}{4\pi} r^{-3} \left(-m_\alpha^{(1)} + 3r^{-2} \left[x_\beta m_\beta^{(1)} \right] x_\alpha \right) \tag{2.18}$$

and

$$b_\alpha^{(8)} = \frac{\mu_0}{8\pi} r^{-5} \left(3m_{\alpha\beta\beta}^{(3)} - 15r^{-2} \left[x_\alpha x_\beta m_{\beta\gamma\gamma}^{(3)} + x_\beta x_\gamma m_{\alpha\beta\gamma}^{(3)} \right] + 35r^{-4} x_\alpha x_\beta x_\gamma x_\delta m_{\beta\gamma\delta}^{(3)} \right) \tag{2.19}$$

where $m_\alpha^{(1)}$ is the dipole moment vector, and $m_{\alpha\beta\gamma}^{(3)}$ is the rank 3 octupole moment tensor. Note that there is no monopole field term, as expected, and that the quadrupole term is missing. The disappearance of the latter and, in fact all even multipole moments ($m^{(2n)}$, n an integer), derives from the restrictions on the magnetization of the body, $\vec{M'}$, together with the axial and fore-aft symmetry of the spheroid.

The dipole moment is given by

$$m_\alpha^{(1)} = M_\alpha' V' \qquad \alpha = 1,2,3 \tag{2.20}$$

where V' is the spheroid volume. For the octupole moment tensor, only 10 of the 27 elements are independent and axial symmetry reduces that number to 6. These are

$$m_{111}^{(3)} = 3m_{221}^{(3)} = 3M_1' I_{11} \ ; \ \ m_{222}^{(3)} = 3m_{112}^{(3)} = 3M_2' I_{11} \ ; \ \ m_{333}^{(3)} = 3M_3' I_{33}$$

$$m_{113}^{(3)} = m_{223}^{(3)} = M_3' I_{11} \ ; \ \ m_{331}^{(3)} = M_1' I_{33} \ ; \ \ m_{332}^{(3)} = M_2' I_{33} \tag{2.21}$$

where

$$I_{11} = \frac{1}{2} \int_{V'} \left(r'^2 - x_3'^2 \right) dv' \ ; \ \ I_{33} = \int_{V'} x_3'^2 dv' \ . \tag{2.22}$$

Note also that

$$m_{\alpha\alpha\beta}^{(3)} = m_{\alpha\beta\alpha}^{(3)} = m_{\beta\alpha\alpha}^{(3)} \tag{2.23}$$

$$m_{\alpha\beta\gamma}^{(3)} = 0 \ \ \text{if} \ \ \alpha \neq \beta \neq \gamma \neq \alpha \ . \tag{2.24}$$

The analysis to this point applies to any axially symmetric body with fore-aft symmetry. We now assume that the body is a spheroid whose symmetry axis length is $2ae$ and whose maximum diameter orthogonal to the symmetry axis is $2a$. It is simple to show that

$$V' = \frac{4}{3}\pi ea^3 \ ; \ \ I_{11} = \frac{4\pi}{15} ea^5 \ ; \ \ I_{33} = \frac{4\pi}{15} e^3 a^5 \tag{2.25}$$

Assume that the external magnetic field (usually the earth's) in the absence of the spheroid is $\vec{b_0} = (b_{01}, b_{02}, b_{03})^T$. A solution of the boundary value problem yields [12]

$$M_j' = \mu_0^{-1} F_j b_{0j} \ \ j = 1,2,3 \tag{2.26}$$

The demagnetization factors F_j are given by

$$F_j = (\mu_{r1} - 1) / (1 + A_j [\mu_{r1} - \mu_{r2}] / [2\mu_{r2}]) \tag{2.27}$$

$$A_1 = A_2 = e\,(e + E)\left(e^2 - 1\right)^{-1} \quad ; \quad A_3 = -2e\left(e^{-1} + E\right)\left(e^2 - 1\right)^{-1} \qquad (2.28)$$

$$E = \ln\left(e - \left[e^2 - 1\right]^{\frac{1}{2}}\right)\left(e^2 - 1\right)^{-\frac{1}{2}} \quad \text{for } e > 1 \quad \text{(prolate)} \qquad (2.29)$$

$$E = \left(\arctan\left[\cdot\left\{1 - e^2\right\}^{-\frac{1}{2}}\right] - \pi/2\right)\left(1 - e^2\right)^{-\frac{1}{2}} \quad \text{for } e < 1 \quad \text{(oblate)} \qquad (2.30)$$

$$A_1 = A_2 = A_3 = \frac{2}{3} \quad \text{for } e = 1 \quad \text{(sphere)} \qquad (2.31)$$

Field quantities have been derived in the body-fixed coordinate system whereas quantities are needed in the space-fixed system in which measurements are made. A body-fixed vector $\vec{u}$ and its related space-fixed vector $\vec{U}$ are connected by the relation

$$\vec{u} = \mathbf{A}\vec{U} \qquad (2.32)$$

where $\mathbf{A}$ is the well known Euler rotation tensor corresponding to Euler angles $(\phi, \theta, 0)$.

Equations 2.17 through 2.32 allow one to calculate the magnetic field $\vec{B}$ at a point in space due to the presence of the spheroid, given the size and shape of the spheroid (a, e), the magnetic material properties of the spheroid and the surrounding medium (μ_{r1}, μ_{r2}), the location of the geometric center of the spheroid $\vec{X}_0$ and the orientation of the spheroid's symmetry axis with respect to the space fixed system (θ, ϕ). However, the equations are insensitive to (μ_{r1}, μ_{r2}) provided $\mu_{r1}/\mu_{r2} > \sim 100$. This is generally the case for ferrous materials in the earth's field. For all model calculations done in this study, we have chosen $\mu_{r1} = 1000$, $\mu_{r2} = 1$, which are typical values encountered in practice.

In addition, Equations 2.20 and 2.26 through 2.32 allow the dipole moment of the spheroid in the space-fixed cartesian frame $\vec{M} = (M_1, M_2, M_3)^T$ to be calculated as :

$$\vec{M} = \frac{V}{\mu_0}\begin{pmatrix} \{F_1 + [F_3 - F_1]\sin^2\theta\cos^2\phi\}B_{01} + \{[F_3 - F_1]\cos\theta\sin\theta\cos\phi\}B_{03} \\ \{[F_3 - F_1]\sin^2\theta\cos\phi\sin\phi\}B_{01} + \{[F_3 - F_1]\cos\theta\sin\theta\sin\phi\}B_{03} \\ \{[F_3 - F_1]\cos\theta\sin\theta\cos\phi\}B_{01} + \{F_1 + [F_3 - F_1]\cos^2\theta\}B_{03} \end{pmatrix}.$$
$$(2.33)$$

3. Experimental Method

3.1 The Smart Magnetometer

To obtain magnetic data as a function of position in a plane, a novel instrument has been developed, which has been dubbed the "smart magnetometer". It collects simultaneous magnetic and position data and estimates location and identity of compact, axially symmetric, ferrous objects. The instrument is self-contained and can be used in a person-portable or vehicle-mounted role.

The second generation of the instrument was used in this study. It is shown in Fig. 3.1.

The major components are a total field magnetometer, a tricycle cart which holds the magnetometer sensor head and has a front wheel-mounted shaft encoder serving as a linear position sensor, a Motorola 68332 EVB microcontroller, an interface between the magnetometer and position encoder signals and the microcontroller and a lap-top computer. Power to the entire system can be supplied by the magnetometer battery pack, but for convenience during the many experiments described here, a DC power supply was used. Interconnections between the electronic components is shown in Figure 3.2, while details of the smart magnetometer interface are shown in Figure 3.3.

A model V101 self-oscillating cesium vapour magnetometer, made by Scintrex, Concord, ON, Canada, is used to obtain the magnetic data. It has a precision due to quantization error for a given sensor head orientation of ± 0.1 nT over a nominal range of 20000 nT to 100000 nT. The accuracy, limited by heading error, is a function of the relative orientation of sensor optical axis and ambient field direction. It is no worse than ± 0.5 nT.

The magnetometer takes 45 ms to make a field measurement and provides a digital BCD output that is updated every 89ms. The magnetometer output is buffered and fed to parallel digital input ports of the microcontroller. As well, the two phase outputs from the position encoder are fed to the input of an advanced timer/counter unit (TPU) on the microcontroller. The position encoder interrupts the microcontroller and increments or decrements a register 2000 times for each revolution of the front cart wheel. (The TPU compares the relative phases of the encoder signals to determine the direction of motion of the wheel and correspondingly increments or decrements the register.) The wheel circumference of 0.618 m then corresponds to a limiting positional resolution of 0.309 mm. However, the effective resolution is governed by the magnetometer field measurement time,

Figure 3.1

Second generation "smart magnetometer". The tricycle cart is on the
left. The position encoder is attached to the front wheel of the cart. The
magnetometer consists of a display box on the right, a cylindrical sensor
head which is attached to the main rod of the cart and an amplifier and
signal conditioning unit and battery pack which are not visible. The lap
top computer is in the center of the photograph, but the microcontroller
is hidden from view.

Magnetometer Sense Head

Magnetometer Amplifier and Signal Conditioning Unit

Optical Encoder

Smart Magnetometer Interface

Power Supply

MC68332 EVB

Magnetometer Control Box
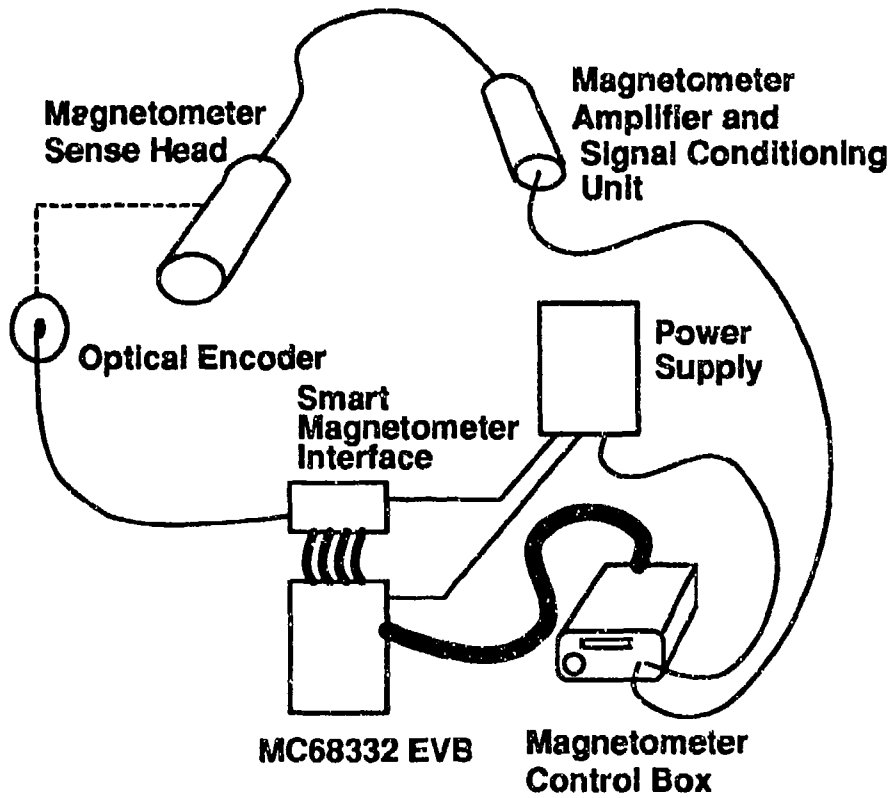
Smart Magnetometer Block Diagram

Figure 3.2

Electrical connections between components of the smart magnetometer.
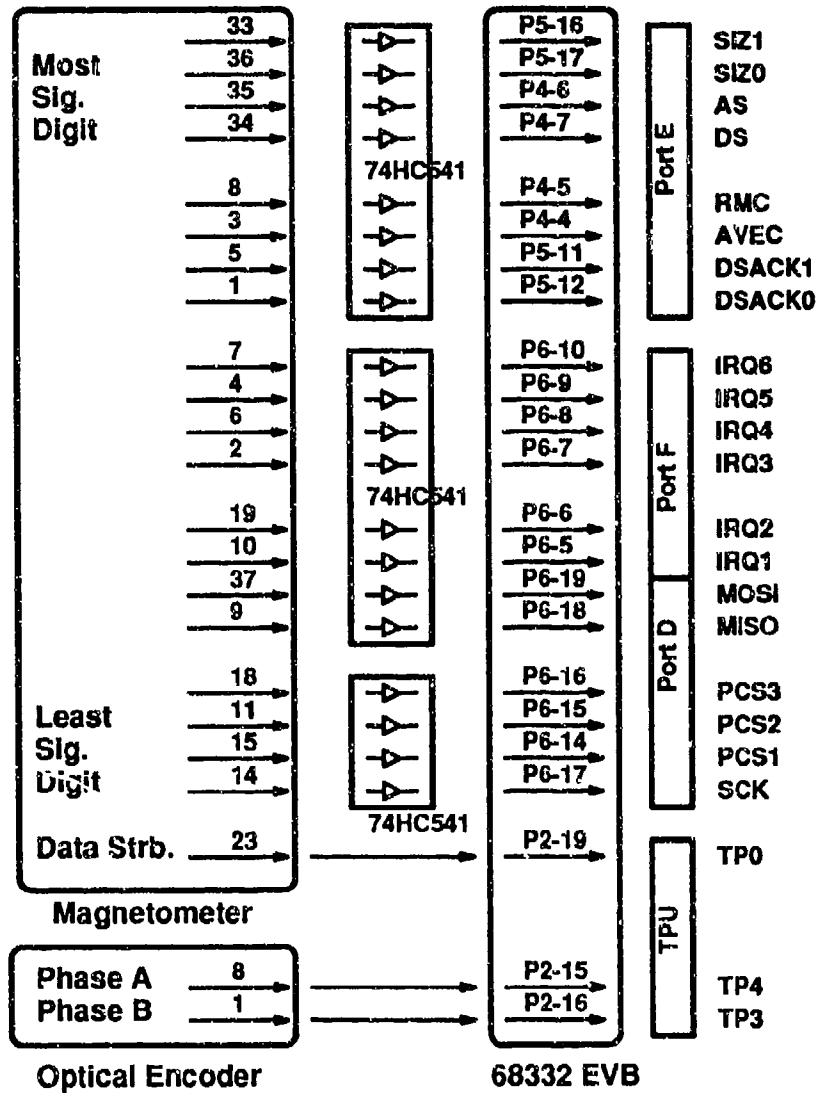
Smart Magnetometer Interface

Figure 3.3

Smart magnetometer interface. Interface buffers signals between the magnetometer and position encoder on the left and the microcontroller on the right. Magnetometer and microcontroller signal names are those used by their respective manufacturers [13], [14].

since the magnetic field value is uncertain within this time period. The effective positional resolution in the direction of motion is thus dependent on cart speed and is 1.125 cm at 0.25 m/sec and 1.350 cm at 0.30 m/sec. The software running on the microcontroller reads the magnetic field ports, converts the values to a magnetic field and then reads the position register whenever the magnetometer outputs a new value. The magnetic field conversion time is less than the spacing between encoder interrupts ($\sim$ 1 msec at 0.3 m/sec) and so the position value corresponds to the position at which the magnetometer signalled that it had acquired the magnetic value. The magnetic field value and the current position value are stored if a predetermined distance has been spanned since the last update.

The microcontroller is the heart of the instrument. It controls collection of magnetic and position data and algorithm execution. The menu-driven software has the following modes:

- Free running - Gives bar graph indication of field strength. Allows the operator to find regions which have magnetic field values of sufficient strength and spatial extent to warrant further investigation.

- Locate - Instructs the operator when and where to make magnetic field and position measurements. Estimates location and moment of the dipole associated with a detected object from the field measurements using the noniterative algorithm of Section 2.2.

- Identify - Identifies detected object from its dipole moment, estimated from the "Locate" mode, using the pattern classifier of Section 2.3.

- Design set update - If the identification was carried out on a known object, this mode uses the results to modify or add a feature vector to the design set.

- Magnetic map transfer - Allows magnetic maps to be transferred to the lap top computer hard disk.

- Design set transfer - Allows design sets to be transferred to/from the lap top computer hard disk.

The lap top computer is initially used to down load code to the microcontroller and acts as a file server for magnetic/position data and design sets for experimental purposes. In an fielded instrument, code can reside permanently on the microcontroller EPROM and the lap top can be replaced by a hand-held terminal or notebook computer.

The location algorithm execution time is a function of how finely the field is sampled in the plane above the object of interest because this determines how many magnetic data values must be searched to find the extrema positions. The location algorithm executed in five seconds for a 170 cm ($\sim$2 cm sample increments) by 210 cm (5 cm sample increments) grid ($\sim$ 3800 total data points in the magnetic map). Execution time for the identification algorithm, which is independent of magnetic map size, took about 30 seconds for a 6 object

design set. These times are still small compared to the data collection time. It took 6 minutes to collect the data for a 170 cm (~2 cm sample increments) by 210 cm (10 cm sample increments) grid and 13 minutes for a 170 cm (~2 cm sample increments) by 210 cm (5 cm sample increments) grid.

3.2 Experimental Layout

Measurements were made in the Threat Detection Group's nonmetallic laboratory which has been described in detail in [7]. The laboratory is a 12 m diameter hemispherical nonmetallic building with minimal metal content. Magnetic field gradients are typically no greater than 1 or 2 nT/m in the usable portions of the building. Magnetic field fluctuations are limited by geomagnetic noise and were typically ±1-2 nT/hour during the time of day in which measurements were made (mid-morning, early afternoon). In the time necessary to measure a magnetic field map (~15 minutes or less), background noise fluctuations were less than the quantization error of magnetic data received by the microcontroller (1 nT) and thus no reference magnetometer was used for background subtraction. The experimental set-up is shown schematically in Fig 3.4.

The measurement table on which the magnetometer moves was situated in a low gradient part of the laboratory. The table was made of wood with brass screws and was heavily reinforced to ensure negligible displacement of the measurement surface when walked on. The horizontal measurement surface was 3.66 m on a side and was 1.04 m above the floor. The table surface was painted in alternating light and dark coloured guide lines spaced 4.8 cm apart. The table was oriented so that the guide lines ran along a direction 5° from a north-south direction (Fig. 3.4). This direction was labelled X_1. The horizontal direction orthogonal to the X_1 direction was labelled X_2. A start line, parallel to the X_2 direction, was situated at either end of the table. Because of practical considerations such as the finite size of the magnetometer cart, placement of the start lines and positioning of the operator, the usable region of the measurement surface was about 2.7m in the X_1 direction and 2.55m in the X_2 direction. The intersection of the lower start line and the left-most guide line was considered to be (0,0, -0.24m) in the space-fixed coordinate system since the nominal center of the magnetometer active volume was 24 cm above the table surface.

The object of interest was placed in a wooden holder that allowed the object to be rotated independently about a vertical or horizontal axis and locked at a desired orientation. The geometric center of the object of interest was then placed directly below the center of the measurement table at a variable depth and orientation. The orientation of the object was defined by two angles. The polar angle, θ, was the angle between the X_3 (vertical) direction and the symmetry axis of the object. The azimuthal angle, ϕ, was the angle between the north-south direction and the projection of the symmetry axis on the $X_1 X_2$ (horizontal) plane.

A separate wooden table, on which the electronics was placed, was situated roughly 2 m from the measurement table. Although all of the electronics could have been carried by
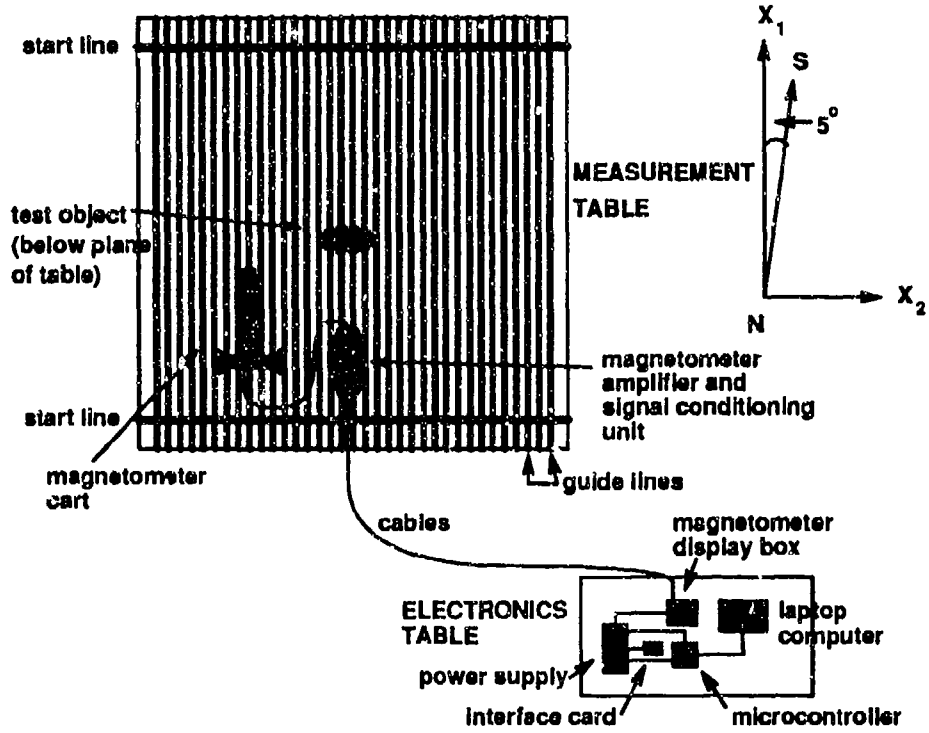
Figure 3.4

Top view of the experimental set-up for measurement of magnetic fields of compact objects.

the operator, it was felt better for experimental purposes to keep the components separate for ease of modification and to keep them distant from the measurement surface to ensure that stray magnetic fields from the electronics would not interfere with the magnetometer sensor. Because of cable length restrictions, the magnetometer electronics box was kept on the measurement table approximately 0.5 m from the magnetometer cart.

3.3   Procedure

To collect a magnetic map the following procedure was used. Prior to collecting the initial map, the electronics were connected, powered up and allowed to stabilize for at least ten minutes. The operator removed all metal and placed it far from the measurement table. The microcontroller code was downloaded from the lap top computer and the program was initiated. For all maps, the object of interest was placed in the appropriate position and orientation. The magnetometer cart was positioned with its rear wheels at the lower start line and its front wheel on the left-most guide line of Figure 3.4 (cart pointing in the positive X_1 direction). The "Locate" mode of the software was selected and initial parameters were entered (X_1, X_2 maximum dimensions, sample spacing). The background magnetic field was sampled for approximately 2 seconds and then a tone signalled the operator to roll the cart with the front wheel running along the guide line. Data would not be collected until the wheels started to roll. While rolling, simultaneous magnetic and position information were automatically acquired. When the microcontroller sensed that sufficient distance had been traversed, data collection was halted and the operator was signalled to stop. The set of position and magnetic data collected along a guide line is called a "scan" or a "scan line". The operator then set the cart with its rear wheels at the upper start line and its front wheel on the next guide line in the positive X_2 direction (cart pointing in the negative X_1 direction). The software had a built-in delay during which data collection was suspended to allow such positioning of the cart. The microcontroller would then signal the operator to commence rolling the cart. (Note that the microcontroller software can use the wheel position encoder to guide the magnetometer to the start of the next X_1 scan. This is not as accurate as using well defined guidelines and starting points and so this feature was not used for these experiments.) The procedure was repeated and a two dimensional array of magnetic values versus X_1, X_2 (which will be called a magnetic map) was acquired in a raster scan fashion until the microcontroller signalled the operator to halt. The location of the object and its associated dipole moment were then estimated and the object was classified. If desired, magnetic data were transferred to hard disk for permanent storage and then the procedure was repeated for a new map.

3.4   Initial Calibration

Prior to commencing the location and identification experiments, a number of magnetic maps were collected to optimize operational procedures and parameters. Yawing of the

se.nsor head was initially noted as a problem, as was an offset between the magnetic sensor head path and the encoder wheel path. Both of these were remedied by modifying the cart.

Optimum scanning speed for the sensor was determined. Because of the fixed temporal spacing between magnetometer outputs, the cart speed had to be adjusted so that the sample spacing was not too large, while still quickly completing a scan. A sample spacing of about 2 cm was desired. It was found that a reasonable sensor speed was roughly 0.30 to 0.25 m/sec. The cart would require 8 to 10 seconds to move from start to finish of one scan line and the microcontroller would store a magnetic field reading every 2.2 to 2.7 cm along the X_1 direction.

A magnetic map was obtained with no object in place, in order to measure the background magnetic field. The map is shown in Figure 3.5. The field gradient is seen to be roughly constant and can be characterized by a single component pointing from the northeast to the southwest corner of the table with magnitude $\sim$ 2 nT/m. The effect of the background is small but significant, particularly for the moment estimation when the magnetic field of the object is weak. Typical examples of the difference in estimation with and without background subtraction are shown in Tables I and II. The object was spheroid "F" (see Table IV for description) in a vertical orientation at depths of 0.598 m (Table I) and 0.802 m (Table II). Peak field value due to the object was $\sim$ 1000nT for Table I and $\sim$ 350nT for Table II. For both Tables, the sample spacing in X_2 direction was 4.8 cm. Seven field maps were used for estimation. Standard deviation for the magnitude is actually the root average square distance (intraset distance) between vectors, based on 7 field maps for Table I and 3 field maps for Table II. The difference in estimates between corrected and uncorrected maps is at most only slightly greater than can be accounted for by the standard deviations for the 0.598 m depth. The difference becomes significantly greater than the statistical uncertainty at a depth of 0.802 m, which is to be expected because of the diminished field due to the object.

In the experiments that follow, the background map was subtracted from the magnetic field map due to the object before applying the location and identification algorithms.

The measurement table guide lines would allow scan lines as close together as 4.8 cm or at any multiple of 4.8 cm. It was desirable to use the closest spacing possible for the study of the location algorithm, but it was necessary to know how sensitive the algorithm estimates were to the X_2 spacing. To test this sensitivity, a set of measurements were made on a fixed object at a fixed orientation. The depth chosen was small (0.39 m) since the estimation should be more sensitive to grid spacing when field maps are narrow as they are at shallow depths. The results are shown in TableIII. The object chosen was spheroid "F" (see Table IV) at $\theta = 90°$, $\phi = 175°$ and at a depth of 0.39 m. Five field maps were used for estimation of 5 cm spacing data and two field maps were used for estimation of the 10 cm spacing data. (These data were obtained on an older, smaller measurement table which had a minimum scan line spacing of 5 cm, rather than 4.8 cm.) The standard deviation for the magnitude is actually the root average square distance. Clearly, there is not a significant difference between the two spacings.

Background on Big Table 16/07/92 PM
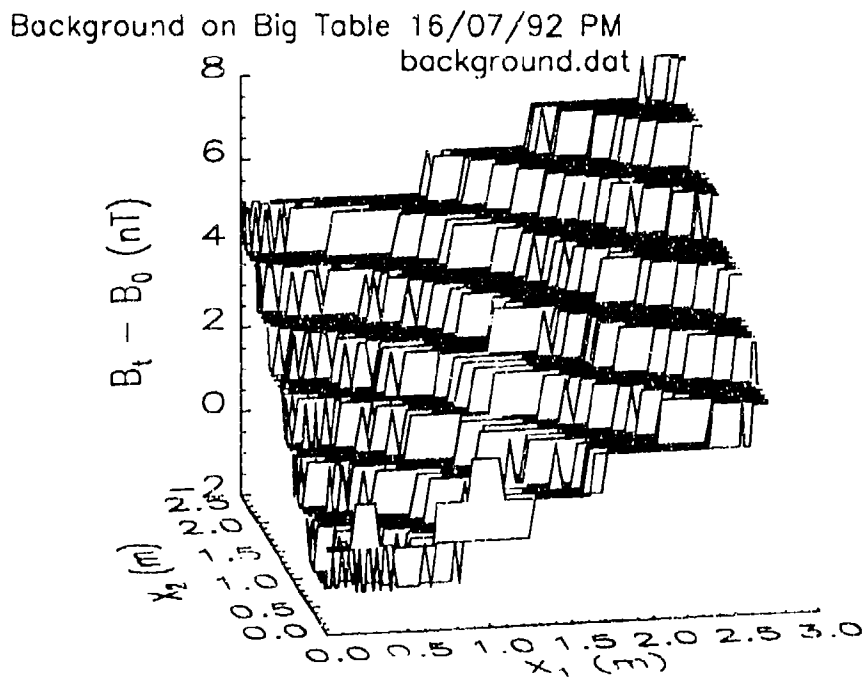
Figure 3.5

Background magnetic map collected by the smart magnetometer on the
measurement table surface.

Component	Uncorrected Map		Corrected Map	
	Mean	Std. Deviation	Mean	Std. Deviation
Location Vector Estimate (m)				
1	1.358	0.010	1.350	0.010
2	1.277	0.001	1.278	0.002
3	-0.540	0.001	-0.554	0.002
magnitude	1.941	0.010	1.940	0.011
Moment Vector Estimate (A·m^2)				
1	0.139	0.035	0.185	0.041
2	0.005	0.003	0.003	0.007
3	0.845	0.008	0.909	0.0188
magnitude	0.857	0.036	0.927	0.046

Table I

Comparison of location and identification estimation results with and without background correction. Object was spheroid "F" in a vertical orientation at a depth of 0.598 m.

Component	Uncorrected Map		Corrected Map	
	Mean	Std. Deviation	Mean	Std. Deviation
Location Vector Estimate (m)				
1	1.383	0.006	1.362	0.006
2	1.322	0.001	1.333	0.001
3	-0.708	0.004	-0.746	0.007
magnitude	2.040	0.007	2.047	0.009
Moment Vector Estimate (A·m^2)				
1	0.077	0.001	0.173	0.023
2	0.008	0.003	0.013	0.005
3	0.774	0.012	0.893	0.022
magnitude	0.778	0.012	0.910	0.033

Table II

Comparison of location and identification estimation results with and without background correction. Object was spheroid "F" in a vertical orientation at a depth of 0.802 m.

Component	5cm Map		10 cm Map	
	Mean	Std. Deviation	Mean	Std. Deviation
Location Vector Estimate (m)				
1	0.865	0.007	0.865	0.012
2	1.058	0.009	1.066	0.019
3	-0.415	0.007	-0.422	0.027
magnitude	1.428	0.019	1.437	0.035
Moment Vector Estimate ($A \cdot m^2$)				
1	0.266	0.020	0.275	0.033
2	-0.004	0.017	-0.002	0.038
3	0.215	0.011	0.216	0.028
magnitude	0.342	0.028	0.349	0.058

Table III

Comparison of location and identification estimation results for magnetic maps collected with an X_2 spacing between scans of 5 cm and 10 cm. Object was spheroid "F" at $\theta = 90°$ and $\phi = 175°$ at a depth of 0.39 m.

4. Experimental Results

Using the experimental method of the last Chapter, magnetic maps were obtained for two mild steel solid spheroids for a variety of depths and orientations. The two objects are summarized in Table IV. Both objects are typical of the size and shape of unexploded ordnance. In the following discussion, the type of spheroid and its orientation for a particular experiment will be designated by a letter (assigned for historical reasons) and two integers. For example, M 90 175 refers to the type "M" spheroid with a polar angle of 90° and azimuthal angle 175°. The orientation for a vertical spheroid is denoted 0 0, even though the azimuthal angle is, strictly speaking, undefined. The orientation angles are defined in Section 3.2.

Figures 4.1 to 4.4 are typical of the variation of magnetic field maps for a single object for different orientations. Both the maximum field value and the relative position of the maximum and minimum field value change with orientation. The maximum field value is seen to decrease with increasing polar angle. This illustrates that simple location schemes which assume that the object center is directly under the maximum field position will have serious errors as will simple identification schemes which use only the maximum field value as a feature.

The location estimates for all experiments are given in Table V. The dipole moment estimates for all experiments are given in Table VI. For both tables, where multiple experiments were done for identical conditions, the standard deviations are given. Note that the range of depths is from 0.39 m to 0.802 m. The lower limit was mainly imposed by the measurement table surface thickness plus magnetometer height plus minimum object dimension ($\sim 4 + 24 + 10.5$ cm respectively), while the upper limit was set by the requirement to have a sufficient signal-to-noise ratio (SNR) to get reasonable precision for the spheroids studied.

It is necessary to characterize both the precision and the accuracy of the location algorithm. To determine the precision or repeatability, one can look at the location and dipole moment estimates for independent magnetic maps that were obtained for the same object, orientation and depth. Precision of a location vector component was measured by the standard deviation of the component, expressed as a fraction of the depth, while precision of a moment vector component was measured by the standard deviation of the component, expressed as a percentage of the average magnitude of the vector. A good measure of the deviation of vectors sampled from the same population is the intraset distance. Given a set

Object Label	Type	$a(m)$	e
F	Prolate Spheroid	0.0525	3.5
M	Prolate Spheroid	0.05896	2.0

Table IV

Two objects used for experiments. Spheroid dimensions are defined in Figure 2.2
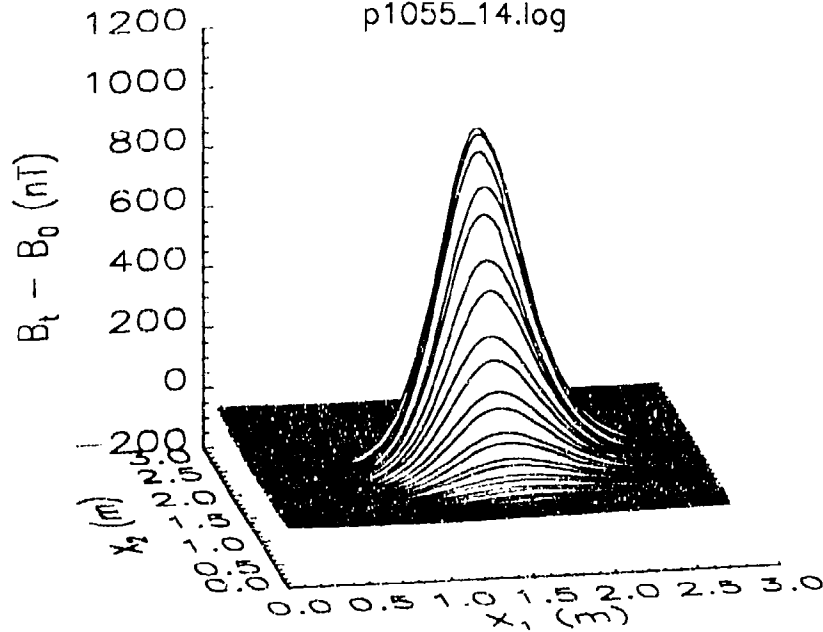
Figure 4.1

Measured total magnetostatic field map versus position in a horizontal plane for spheroid F at $\theta = 0°$. Depth is 0.598 m. Ambient (earth's) field magnitude has been subtracted.

Prolate Spheroid F 30 175 d=0.525m 06/08/92 PM
aug6_2.dat
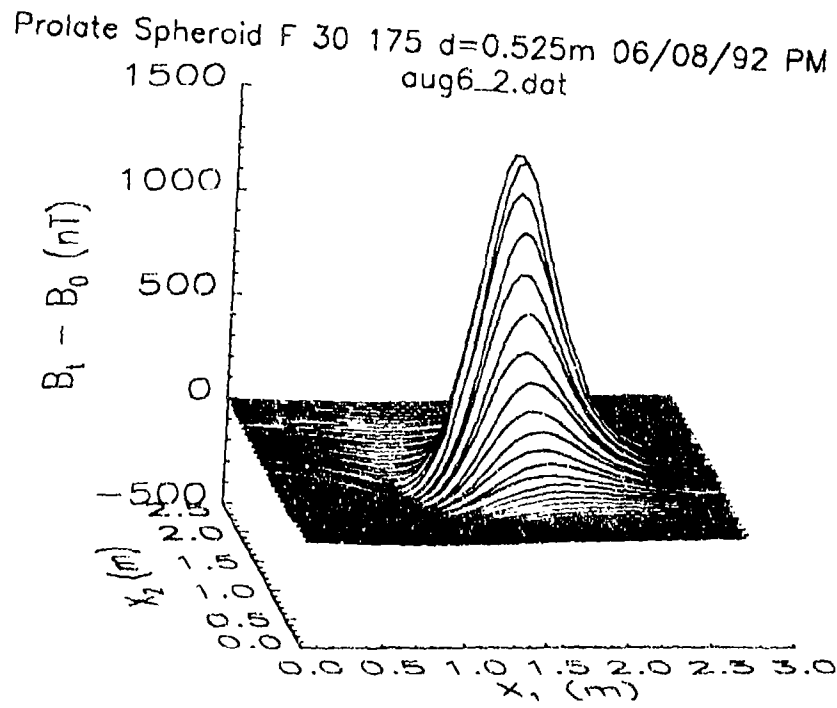
Figure 4.2

Measured total magnetostatic field map versus position in a horizontal plane for spheroid F at $\theta = 30°$ and $\phi = 175°$. Depth is 0.525 m. Ambient (earth's) field magnitude has been subtracted.

Prolate Spheroid F 60 175 d=0.525m 06/08/92 PM
aug6_1.dat
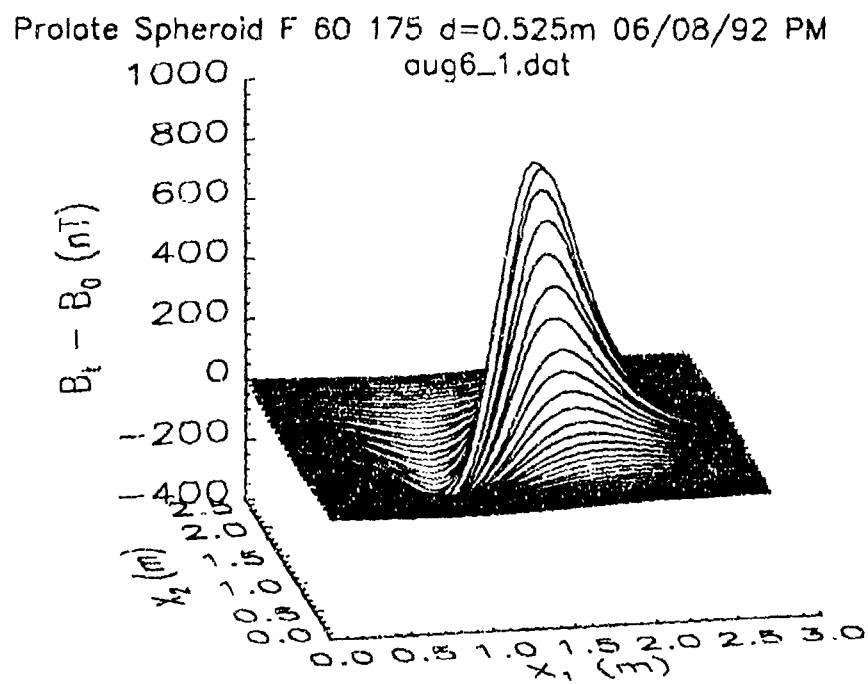
Figure 4.3

Measured total magnetostatic field map versus position in a horizontal plane for spheroid F at $\theta = 60°$ and $\phi = 175°$. Depth is 0.525 m. Ambient (earth's) field magnitude has been subtracted.

DRES-SR-582

Prolate Spheroid F 90 175 d=0.655m 16/07/92 PM
ju16_2.dat
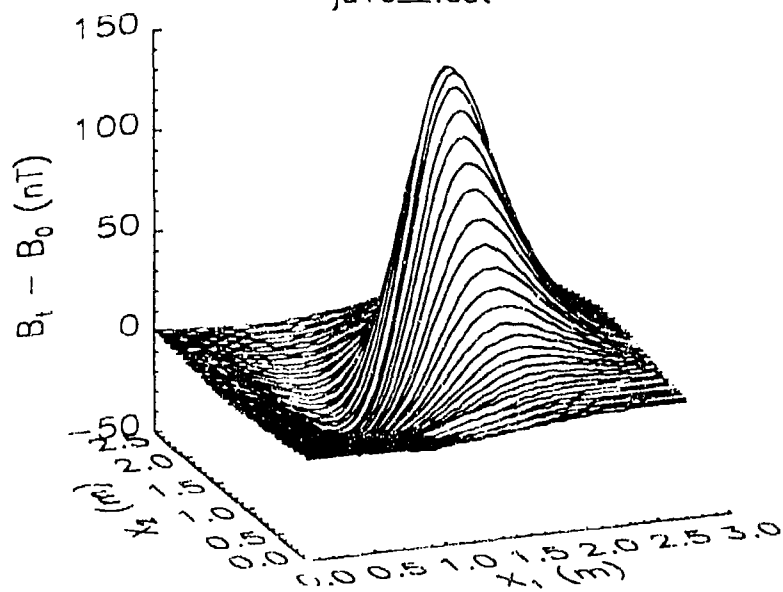
Figure 4.4

Measured total magnetostatic field map versus position in a horizontal plane for spheroid F at $\theta = 90°$ and $\phi = 175°$. Depth is 0.655 m. Ambient (earth's) field magnitude has been subtracted.

Spheroid Type, Orientation	Measured			Estimated		
	X_{01} (m)	X_{02} (m)	X_{03} (m)	X_{01} (m)	X_{02} (m)	X_{03} (m)
F 0 0	0.87	1.04	0.50	0.870	1.05	0.411
	1.321	1.288	0.598	1.350 ± 0.010	1.278 ± 0.002	0.554 ± 0.002
	1.357	1.333	0.698	1.372 ± 0.002	1.317 ± 0.002	0.642 ± 0.000
	1.357	1.333	0.802	1.362 ± 0.006	1.333 ± 0.001	0.746 ± 0.006
	1.347	1.293	0.565	1.344 ± 0.002	1.298 ± 0.000	0.487 ± 0.001
M 10 175	0.87	1.04	0.50	0.862	1.05	0.458
F 90 175	1.362	1.313	0.525	1.368	1.311	0.534
	0.855	1.04	0.390	0.865 ± 0.007	1.058 ± 0.009	0.415 ± 0.007
	0.87	1.04	0.440	0.894	1.050	0.504
	1.36	1.33	0.655	1.391	1.306	0.676
F 60 175	1.362	1.313	0.525	1.392	1.307	0.539
F 30 175	1.362	1.313	0.525	1.405	1.301	0.494
F 60 265	1.362	1.313	0.525	1.408	1.316	0.556
F 30 265	1.362	1.313	0.525	1.389	1.326	0.499
M 90 265	0.87	1.04	0.438	0.884 ± 0.005	1.040 ± 0.001	0.453 ± 0.007
	0.87	1.04	0.468	0.877	1.070	0.455
	0.91	0.97	0.580	0.938	1.003	0.524

Table V

Location estimation results using experimental data from spheroids. Where multiple experiments have been done under identical conditions, standard deviations are given.

Spheroid Type, Orientation	depth (m)	Mathematical Model			Estimated		
		M_1 (A·m^2)	M_2 (A·m^2)	M_3 (A·m^2)	M_1 (A·m^2)	M_2 (A·m^2)	M_3 (A·m^2)
F 0 0	0.500	0.065	0.000	1.069	0.072	0.001	0.716
	0.698	0.065	0.000	1.069	0.177 ± 0.005	0.013 ± 0.013	0.876 ± 0.001
	0.565	0.065	0.000	1.069	0.161 ± 0.003	-0.009 ± 0.001	0.701 ± 0.002
	0.598	0.065	0.000	1.069	0.185 ± 0.042	0.003 ± 0.007	0.909 ± 0.019
	0.802	0.065	0.000	1.069	0.173 ± 0.023	0.013 ± 0.005	0.893 ± 0.022
F 90 175	0.390	0.325	-0.023	0.212	0.266 ± 0.020	-0.004 ± 0.017	0.215 ± 0.011
	0.440	0.325	-0.023	0.212	0.315	-0.001	0.245
	0.655	0.325	-0.023	0.212	0.238	-0.015	0.182
	0.525	0.325	-0.023	0.212	0.410	-0.035	0.191
M 90 265	0.438	0.059	0.007	0.189	0.082 ± 0.006	-0.061 ± 0.001	0.158 ± 0.007
	0.468	0.059	0.007	0.189	0.039	0.029	0.105
	0.580	0.059	0.007	0.189	0.028	-0.003	0.123
F 60 175	0.530	0.621	-0.049	0.539	0.779	-0.062	0.550
F 30 175	0.525	0.499	-0.038	0.967	0.554	-0.040	0.833
F 60 265	0.525	0.099	0.386	0.436	0.137	0.495	0.541
F 30 265	0.525	0.098	0.375	0.864	0.169	0.028	0.817
M 10 175	0.500	0.105	-0.004	0.455	0.030	-0.003	0.300

Table VI

Dipole moment estimation results using experimental data from
spheroids. Where multiple experiments have been done under identical
conditions, standard deviations are given. Theoretical moment compo-
nent values are obtained from the mathematical model of Section 2.4.

of vectors, $\vec{a}^i, i = 1, ..., K$, the intraset distance, $\overline{D^2}$, is the mean square distance between vectors given by [15]

$$\overline{D^2} = \frac{1}{K(K-1)} \sum_{j=1}^{K} \sum_{i=1}^{K} \sum_{k=1}^{n} (a_k^j - a_k^i)^2 \tag{4.1}$$

where a_k^i is the kth component of $\vec{a}^i$ and $k = 1, ...n$. The precision in estimation of location vectors was taken to be the square root of the intraset distance between individual location vector estimates for a given object, orientation and depth. For two depths, 0.500 m and 0.525 m, different orientations and/or objects were used to determine the precision in depth whereas for other depths, these parameters were constant for a given depth. The precision in estimation of moment vectors was assigned to be the square root of the intraset distance between individual moment vector estimates. Since moments are a function of object type and orientation, precision in moments could not be determined for the 0.500 and 0.525 m depths. The results of the precision in estimation are given in Tables VII and VIII and Figures 4.5 and 4.6.

From Tables VII and VIII and Figures 4.5 and 4.6, it can be seen that the precision in estimating location varies from 0.12 to 1.90%. However, there is also a variation in location estimate with object type and/or orientation, since the two depths with the worst precision (1.67, 1.90%) are the only ones which have different types and orientations included in the precision estimates. If these are excluded, the precision in depth ranges from 0.12 to 1.35%. The precision in estimating the dipole moment varies from 0.51 to 8.21 %. There appears to be a slight increase in uncertainty as depth decreases, but the precision is not closely correlated with the peak magnetic field. This variation in precision may be partly because the widths of the magnetic field maps scale linearly with depth. When sampling with a fixed width sampling grid, estimates will be more sensitive to narrow maps. Also, the lowest depth cases were done for spheroids with a horizontal symmetry axis. The shape of the magnetic map for these cases will differ from those for the remainder which are for vertical axis spheroids (compare Figs. 4.1 and 4.4). The use of a fixed width sampling grid may then again make estimates more sensitive to one orientation than another.

It is also interesting to note that the precision of the dipole moment estimates is always larger than the precision of the location estimates for the same object, orientation and depth. This is as expected, since Equation 2.5 shows that for a given orientation, the magnitude of the moment is equal to the cube of the depth times a constant. Simple error propagation theory then suggests that the percentage error in moment should be three times that in depth. Since error in depth usually dominates the error in the other directions [10], the percentage error in dipole moment should be at least three times the percentage error in location.

Although the precision (repeatability) is quite good, it is also necessary to know what is the accuracy in estimation; that is, are the estimates biased? To get a preliminary assessment of accuracy, the depth estimates averaged over all object types and orientations for a given depth were plotted versus measured depth. The results are presented in Table IX and Figure 4.7

Depth (m)	Spheroid Type, Orientation	Number of Trials	Peak Field (nT)	X_{01} (%)	X_{02} (%)	X_{03} (%)	$\vec{X_0}$ (%)
0.390	F 90 175	5	~600	1.79	2.31	1.79	1.35
0.438	M 90 265	4	~300	1.14	0.23	1.60	0.86
0.500	F,M - -	2	-	0.78	0.12	4.69	1.67
0.525	F - -	5	-	4.27	1.95	5.43	1.90
0.565	F 0 0	2	~1000	0.35	0.00	0.17	0.12
0.598	F 0 0	7	~800	1.67	0.33	0.33	0.56
0.698	F 0 0	2	~600	0.28	0.28	0.00	0.17
0.802	F 0 0	3	~350	0.75	0.12	0.75	0.44

Table VII

Precision in location vector estimation for the location algorithm of Section 2.2 using experimental data. For a given depth, the precision in a component $X_{0i}, i = 1, 2, 3$ is the standard deviation for the component expressed as a percentage of the depth. Precision of the vector $\vec{X_0}$ is the square root of the intraset distance for all vectors at a given depth expressed as a percentage of the vector magnitude. Data at 0.500 and 0.525 m depths includes different orientations and/or objects.

Depth (m)	Spheroid Type, Orientation	Number of Trials	Peak Field (nT)	M_1 (%)	M_2 (%)	M_3 (%)	$\bar{M}$ (%)
0.390	F 90 175	5	~600	5.85	4.97	3.22	8.21
0.438	M 90 265	4	~300	3.20	0.45	3.73	6.65
0.565	F 0 0	2	~1000	0.40	0.13	0.27	0.51
0.598	F 0 0	7	~800	4.54	0.75	2.04	4.97
0.698	F 0 0	2	~600	0.56	1.46	0.11	1.58
0.802	F 0 0	3	~350	2.52	0.53	2.41	2.61

Table VIII

Precision in dipole moment vector estimation for the location algorithm of Section 2.2 using experimental data. For a given depth, the precision in a component M_i, $i = 1, 2, 3$ is the standard deviation for the component expressed as a percentage of the average moment magnitude. Precision of the vector is the the square root of the intraset distance for all vectors of a given object type, orientation and depth, expressed as a percentage of the vector magnitude.

Measured Depth (m)	Estimated Depth (m)	Measured Depth (m)	Estimated Depth (m)
0.390	0.415 ± 0.007	0.565	0.487 ± 0.001
0.438	0.453 ± 0.007	0.580	0.524
0.440	0.504	0.598	0.554 ± 0.002
0.468	0.455	0.655	0.676
0.500	0.435 ± 0.023	0.698	0.642 ± 0.000
0.525	0.525 ± 0.029	0.802	0.746 ± 0.007

Table IX

Spheroid depth estimates as a function of depth for experimental data. All objects and orientations are grouped together for a given depth. Uncertainties (precision) are given if available.
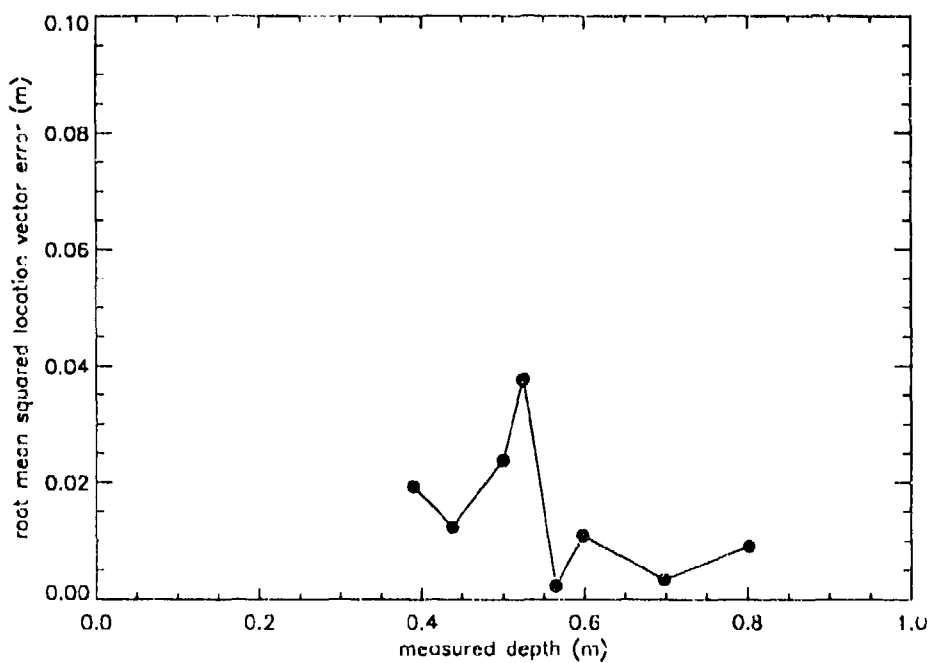
Figure 4.5

Precision in location vector estimation for the location algorithm using experimental data. The precision is the root mean square error for all vectors at a given depth. Data at 0.500 and 0.525 m depths includes different orientations and/or objects.
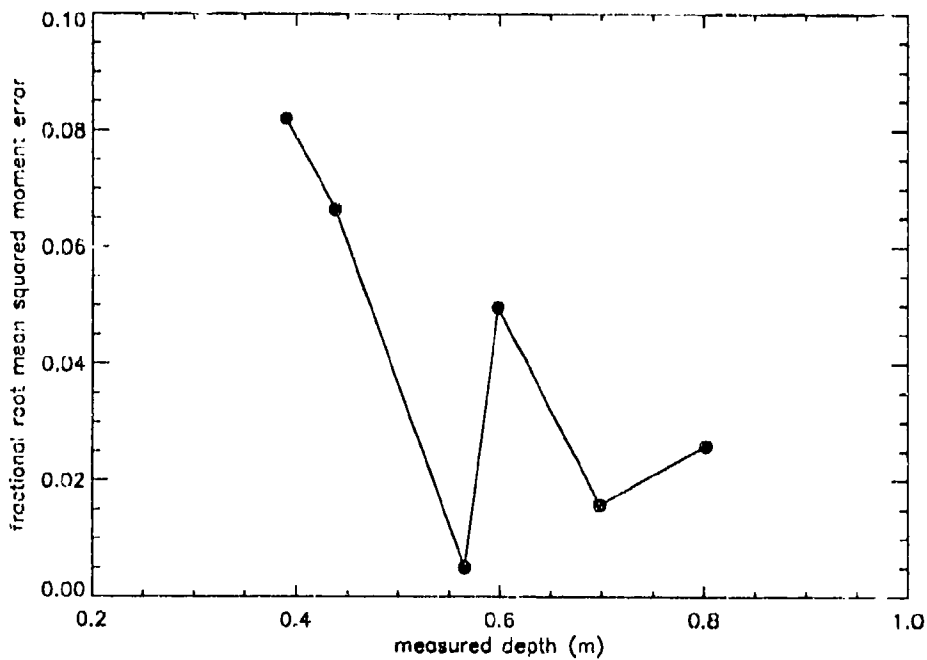
Figure 4.6

Precision in dipole moment vector estimation for the location algorithm using experimental data. The precision is the root me; ' square error for all vectors of a given object type and orientation and dep.h expressed as a fraction of the dipole moment vector magnitude.
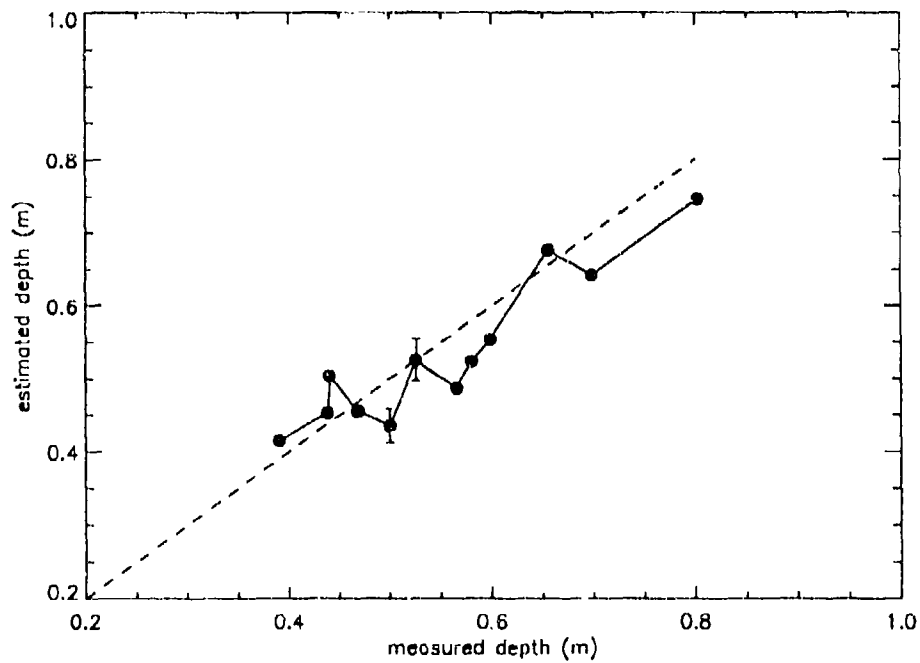
Figure 4.7

Spheroid depth estimates as a function of depth for experimental data.
All objects and orientations are grouped together for a given depth. Un-
certainties are shown where available and are in most cases smaller than
the data points. The dashed line is the line along which data points would
lie if the estimates were unbiased.

From the data, it can be concluded that there is a depth dependent bias in the estimation of depth. The bias is larger than can be explained by statistical fluctuations. In general, depth estimates are slightly high for small depths and slightly low for large depths. If one examines Table V more closely, it can be seen that the algorithm generally underestimates the depth for $\theta \leq 30°$ and overestimates for $\theta \geq 60°$. An exception is the (90 265) orientation for which one depth is underestimated and two are overestimated. It is also interesting to note that the average error in depth is larger for vertical spheroids than it is for higher polar angles (Table V). One explanation is that the negative peak is smaller in magnitude and broader for the vertical case than for larger polar angles, which might make the error in estimating the peak position larger. This can be discounted since, if it were true, the precision in estimates for the vertical spheroid would be worse than for the horizontal spheroid. However, the precision for the two orientations are similar. A more likely explanation is that for a given orientation, the octupole field causes the centroids of the magnetic field to be shifted from the position of the field extrema. This shift will be a function of the ratio of octupole to dipole field values in the measurement plane, which will in turn be dependent on the object orientation. Likewise, the effect of a small amount of remnant magnetization will also be dependent on orientation [7].

To examine the bias in estimation further, it is instructive to look at the bias in estimation of the individual components of the location vector. These are presented in Figures 4.8 to 4.10

It is seen that all three components have a depth dependent bias which is larger than can be accounted for by the precision of the algorithm. The X_{01} component of the location is almost always overestimated. The X_{02} component is generally overestimated for depths less than 0.55 m and underestimated for depths between 0.55 m and 0.8m. Over the limited depth range, the data is consistent with a bias which is periodic with depth, having a 0.25 m period. Further experiments at larger and smaller depths might confirm this. A trend similar to that of the X_{02} component appears to occur for the X_{03} component except that the crossover from overestimation to underestimation occurs at about 0.45 m depth. The data may be consistent with a bias which is periodic with depth, but the uncertainties in estimation make determination of the period difficult. Errors in X_{03} are generally larger than those for X_{01} and X_{02}. The root mean square (rms) error over all depths is 0.020 m for X_{01}, 0.019 m for X_{02} and 0.045 m for X_{03}. This should be compared with the average precision for a fixed object and orientation which is 0.005 m for X_{01}, 0.003 m for X_{02}, and 0.004 m for X_{03}.

Analysing the bias in the estimation of the dipole moments is more difficult, since the "true" moment components cannot be directly measured as can the location components. We can, however, compare the moment component estimates for a fixed object type and orientation with theoretical values obtained from the model of Section 2.4. Figures 4.11 to 4.13 show the variation with depth of the estimates of the three moment components for a type-F spheroid with orientation 0 0. Figures 4.14 to 4.16 show the same thing for a type F spheroid with orientation 90 175 and Figures 4.17 to 4.19 show the variation for a type-M spheroid with orientation 90 265. (Also shown on each Figure are estimates of the
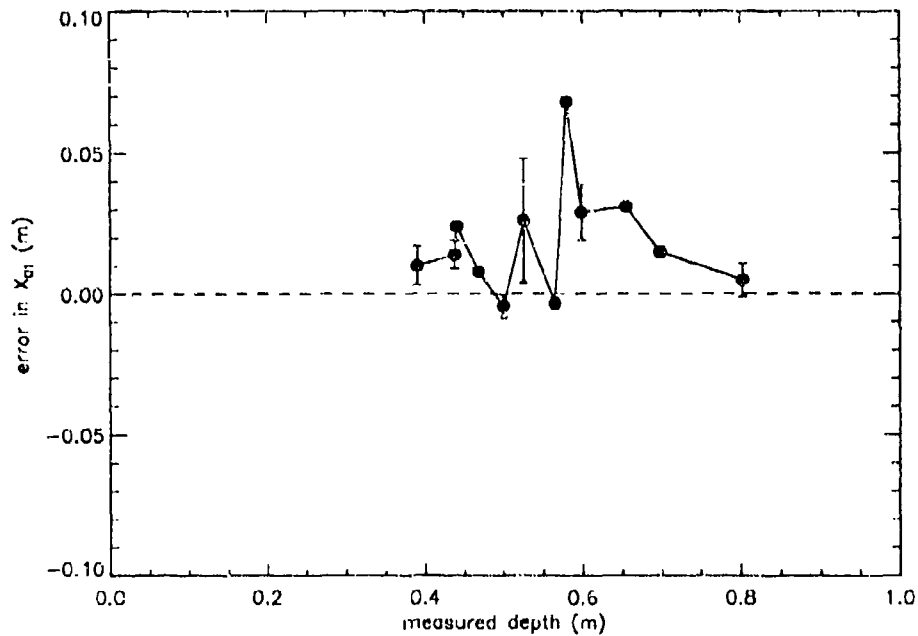
Figure 4.8

Error in estimates of X_{01} component as a function of spheroid depth for experimental data. Error is defined as estimated X_{01} minus measured X_{01}. All objects and orientations are grouped together for a given depth. Uncertainties are shown where available and are in some cases smaller than the data points. The dashed line is the line along which data points would lie if the estimates were unbiased.
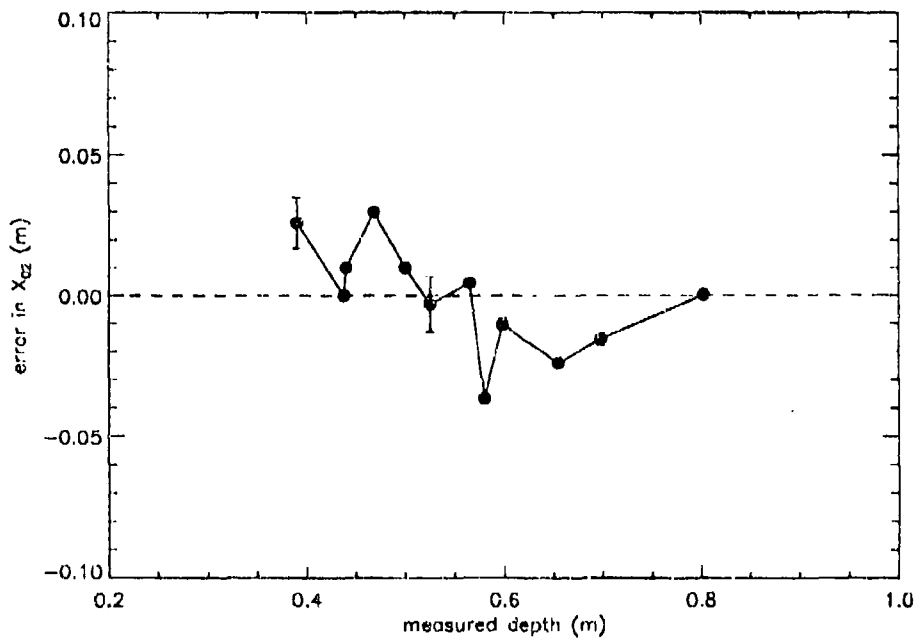
Figure 4.9

Error in estimates of X_{02} component as a function of spheroid depth
for experimental data. Error is defined as estimated component minus
measured component. All objects and orientations are grouped together
for a given depth. Uncertainties are shown where available and are in
some cases smaller than the data points. The dashed line is the line along
which data points would lie if the estimates were unbiased.
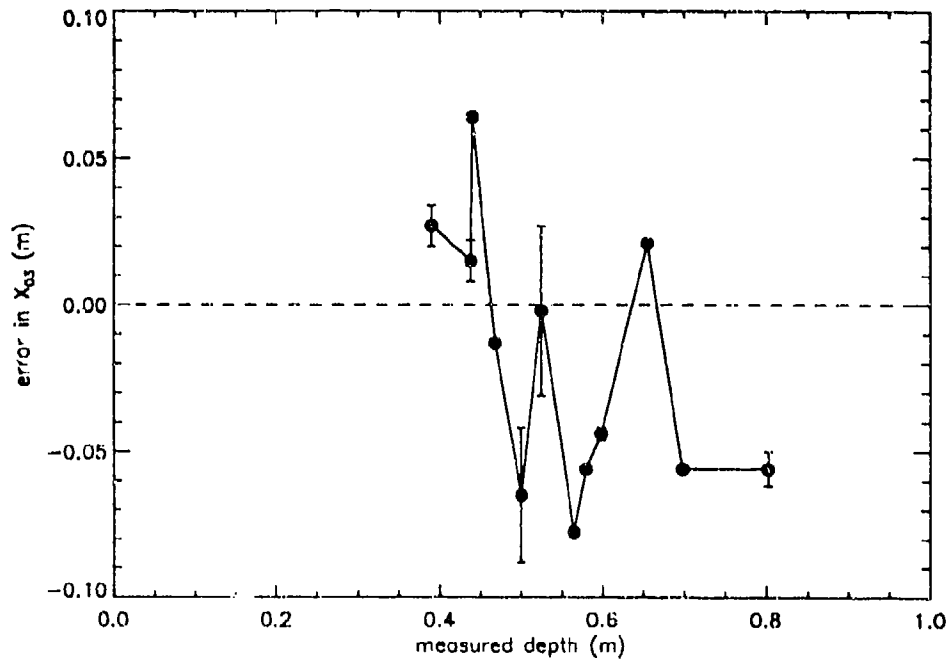
Figure 4.10

Error in estimates of X_{03} component as a function of spheroid depth for experimental data. Error is defined as estimated component minus measured component. All objects and orientations are grouped together for a given depth. Uncertainties are shown where available and are in some cases smaller than the data points. The dashed line is the line along which data points would lie if the estimates were unbiased.

dipole moment components using as input magnetic field maps derived from the model of Section 2.4. Discussion of these will be deferred to the next Chapter.)

A number of points should be noted about Figures 4.11 to 4.19. There is a deviation between theoretical values and experimental estimates that is greater than the uncertainties in the estimates. Within the confines of the limited number of data points, the deviation does not exhibit a clear trend with depth. To explore a possible trend with object type or orientation, the difference between estimated and theoretical moment components, normalized by the magnitude of the theoretical moment, were plotted for various objects and orientations. For multiple estimates of the same object type and orientation at different depths, the unweighted average of estimates at all depths for that object type and orientation was used and the uncertainty in estimate was taken to be the standard deviation of the estimates about the average. These results are shown in Figures 4.20 to 4.23.

The unweighted average difference between estimated and theoretical components as a percentage of the theoretical dipole moment is $4.8 \pm 7.6\%$ for M_1, $-3.3 \pm 15.5\%$ for M_2, $-10.8 \pm 17.5\%$ for M_3 and $24.5 \pm 11.4\%$ for the root vector difference. There is no clear trend with object type or orientation. The sources of the estimation bias will be discussed in the next Chapter.

Figure 4.11

Estimates of M_1 component of the dipole moment as a function of spheroid depth for spheroid F at orientation 0 0. Dots are estimates for experimental magnetic field maps. Stars are for theoretically derived maps (discussed in next Chapter). The dashed line represents the dipole moment component calculated for the object type and orientation, using the model of Section 2.4. Uncertainties are shown where available and are in some cases smaller than the data points.

Figure 4.12

Estimates of M_2 component of the dipole moment as a function of spheroid depth for object F at orientation 0 0. Dots are estimates for experimental magnetic field maps. Stars are for theoretically derived maps (discussed in next Chapter). The dashed line represents the dipole moment component calculated for the object type and orientation, using the model of Section 2.4. Uncertainties are shown where available and are in some cases smaller than the data points.

Figure 4.13

Estimates of M_3 component of the dipole moment as a function of spheroid depth for object F at orientation 0 0. Dots are estimates for experimental magnetic field maps. Stars are for theoretically derived maps (discussed in next Chapter). The dashed line represents the dipole moment component calculated for the object type and orientation, using the model of Section 2.4. Uncertainties are shown where available and are in some cases smaller than the data points.

Figure 4.14

Estimates of M_1 component of the dipole moment as a function of spheroid depth for object F at orientation 90 175. Dots are estimates for experimental magnetic field maps. Stars are for theoretically derived maps (discussed in next Chapter). The dashed line represents the dipole moment component calculated for the object type and orientation, using the model of Section 2.4. Uncertainties are shown where available and are in some cases smaller than the data points.
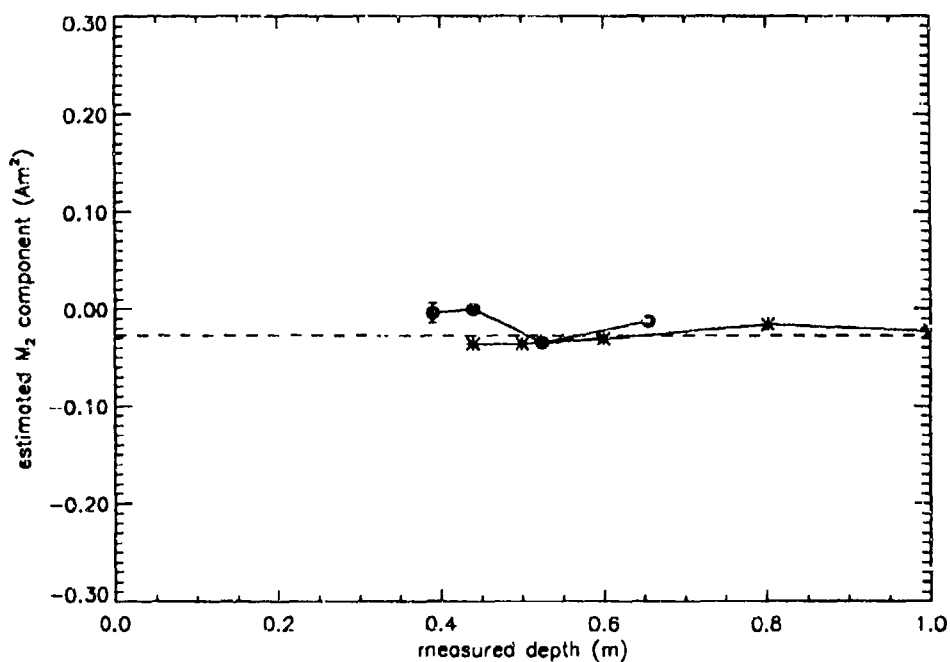
Figure 4.15

Estimates of M_2 component of the dipole moment as a function of spheroid depth for object F at orientation 90 175. Dots are estimates for experimental magnetic field maps. Stars are for theoretically derived maps (discussed in next Chapter). The dashed line represents the dipole moment component calculated for the object type and orientation, using the model of Section 2.4. Uncertainties are shown where available and are in some cases smaller than the data points.
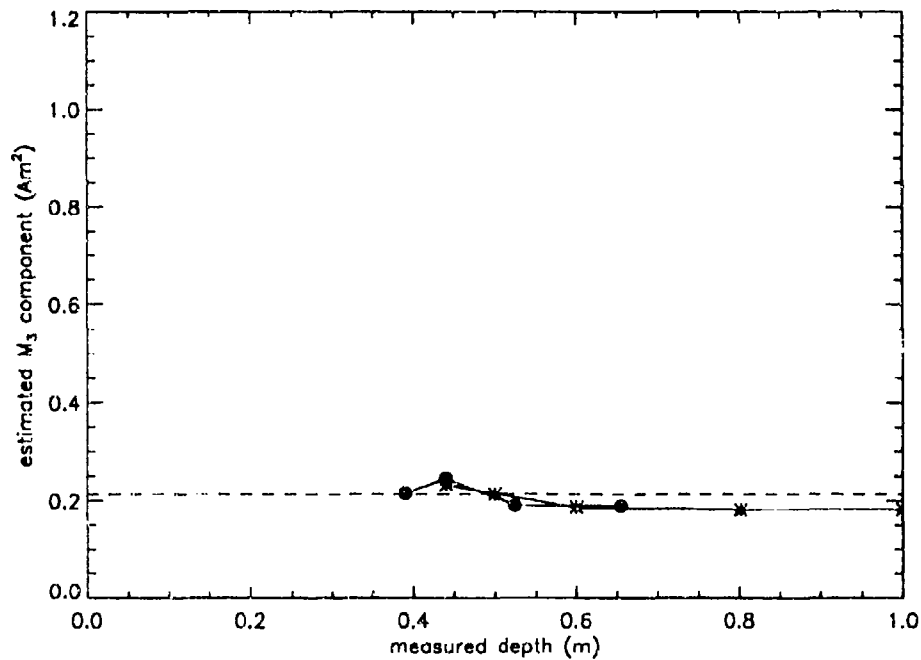
Figure 4.16

Estimates of M_3 component of the dipole moment as a function of spheroid depth for object F at orientation 90 175. Dots are estimates for experimental magnetic field maps. Stars are for theoretically derived maps (discussed in next Chapter). The dashed line represents the dipole moment component calculated for the object type and orientation, using the model of Section 2.4. Uncertainties are shown where available and are in some cases smaller than the data points.
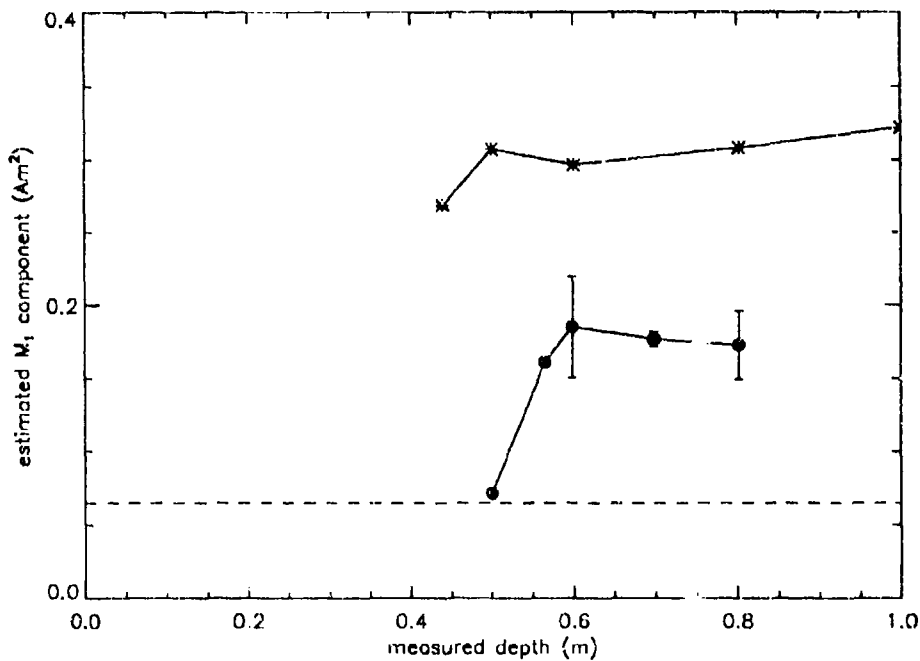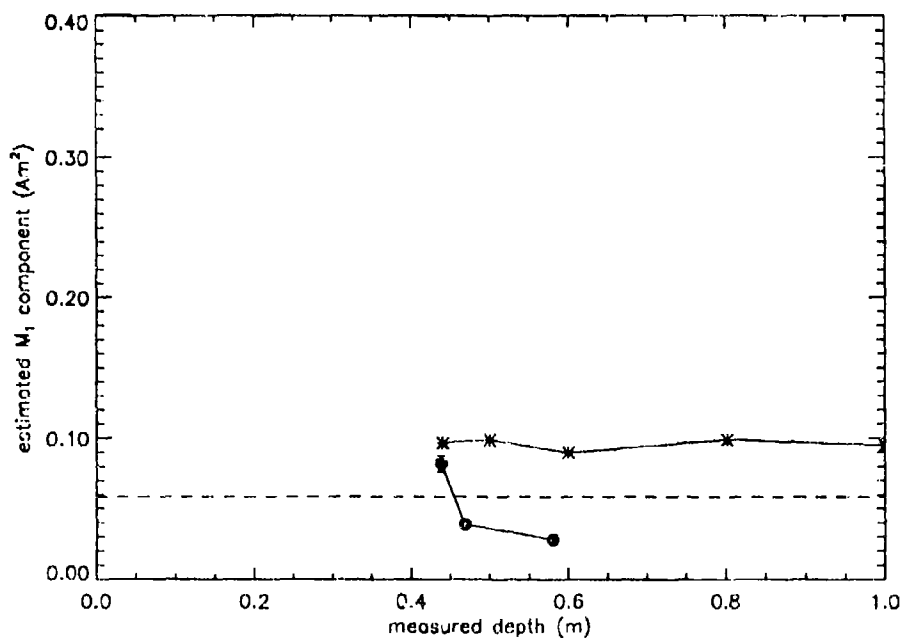
Figure 4.17

Estimates of M_1 component of the dipole moment as a function of spheroid depth for object M at orientation 90 265. Dots are estimates for experimental magnetic field maps. Stars are for theoretically derived maps (discussed in next Chapter). The dashed line represents the dipole moment component calculated for the object type and orientation, using the model of Section 2.4. Uncertainties are shown where available and are in some cases smaller than the data points.
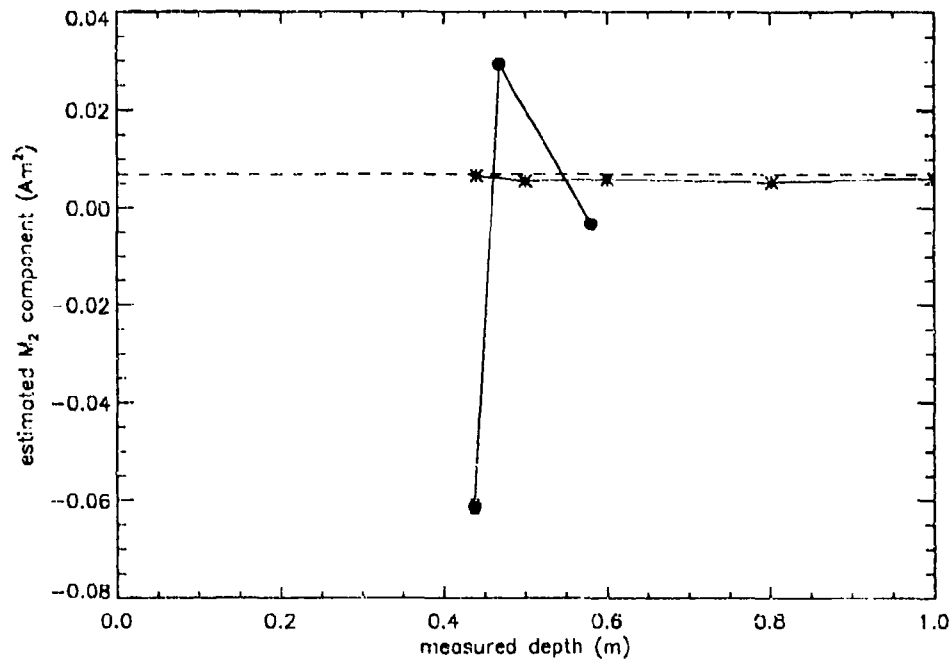
Figure 4.18

Estimates of M_2 component of the dipole moment as a function of spheroid depth for object M at orientation 90 265. Dots are estimates for experimental ma_ etic field maps. Stars are for theoretically derived maps (discussed in next Chapter). The dashed line represents the dipole moment component calculated for the object type and orientation, using the model of Section 2.4. Uncertainties are shown where available and are in some cases smaller than the data points.
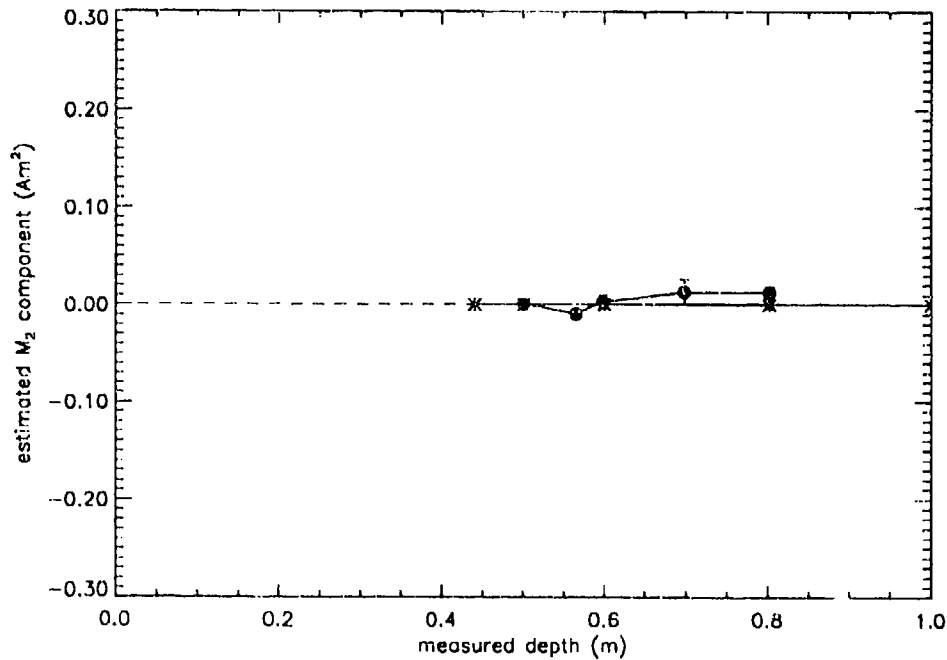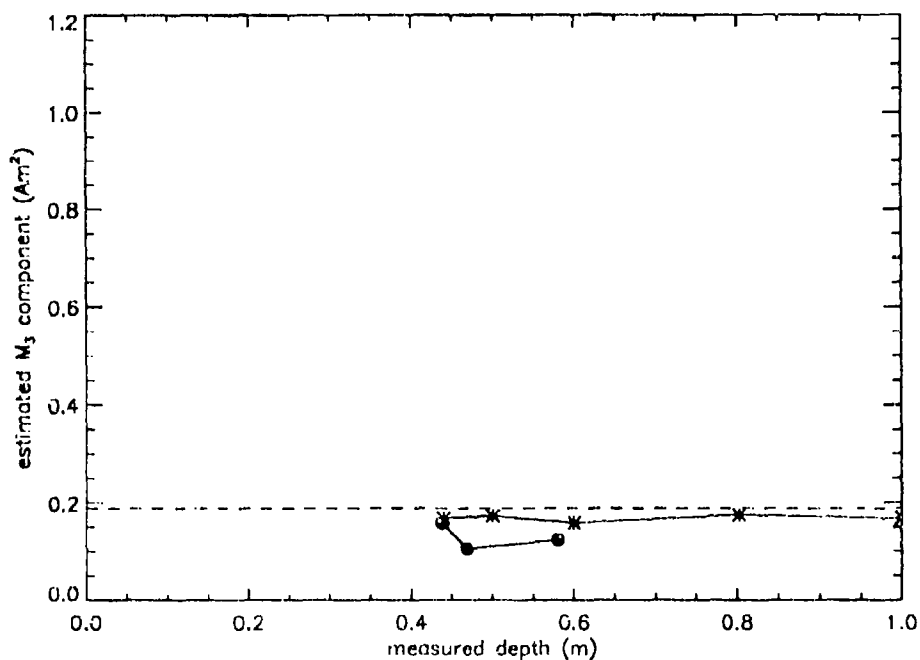
Figure 4.19

Estimates of M_3 component of the dipole moment as a function of spheroid depth for object M at orientation 90 265. Dots are estimates for experimental magnetic field maps. Stars are for theoretically derived maps (discussed in next Chapter). The dashed line represents the dipole moment component calculated for the object type and orientation, using the model of Section 2.4. Uncertainties are shown where available and are in some cases smaller than the data points.
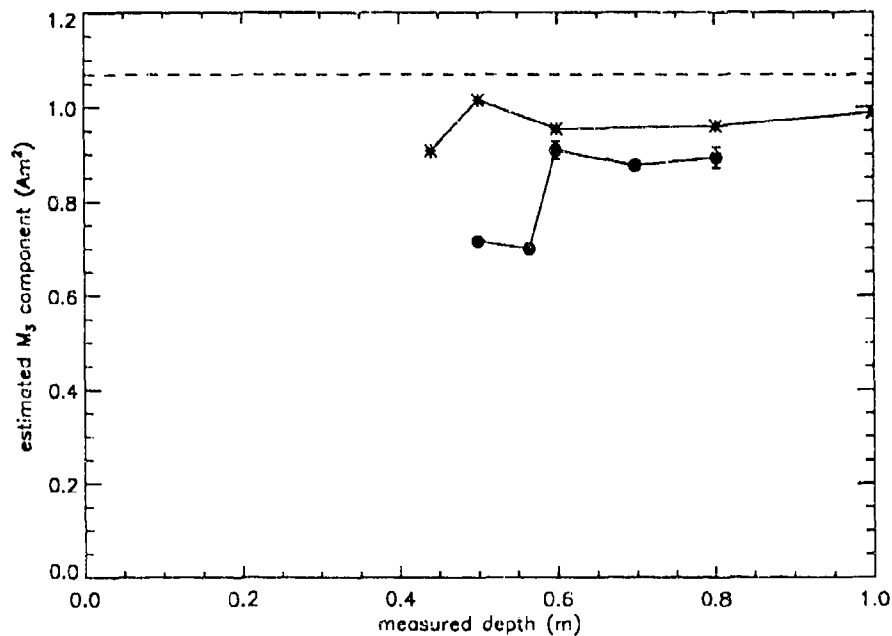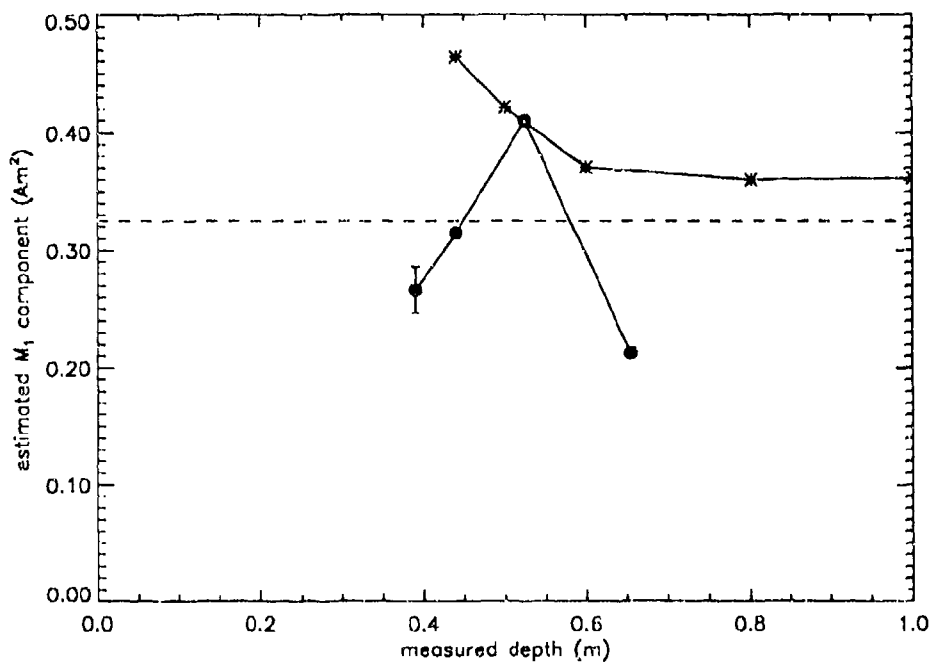
object, orientation
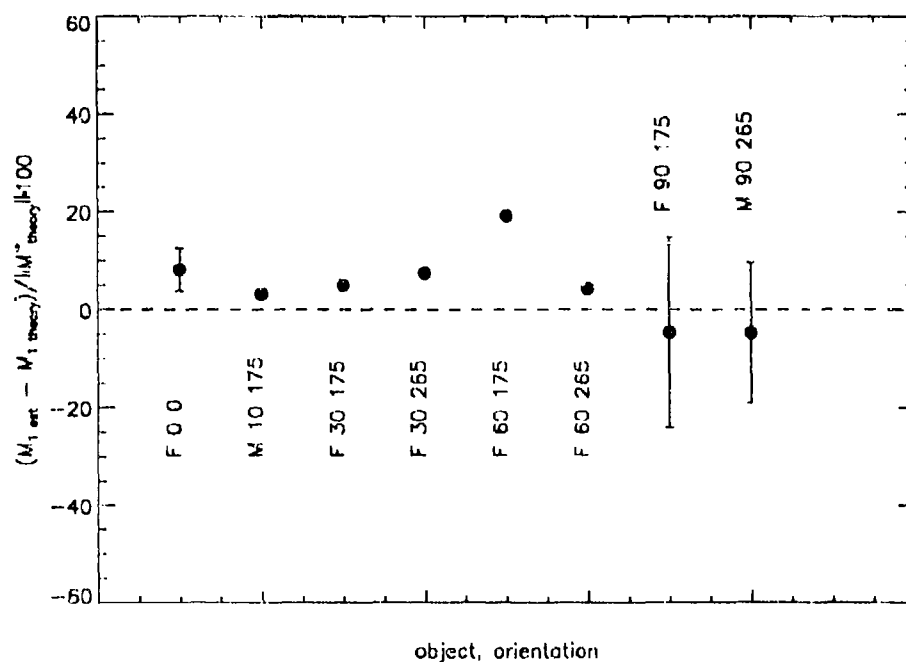
Figure 4.20

Difference between M_1 component estimate and theoretical M_1, as a percentage of the magnitude of theoretical $\vec{M}$ for two different objects and a number of different orientations. Points are labelled with a letter for object type and two numbers. The first gives the polar angle and the second gives the azimuthal angle in degrees. Points with error bars are unweighted averages of a number of estimates at different depths. Error bars are the standard deviations.
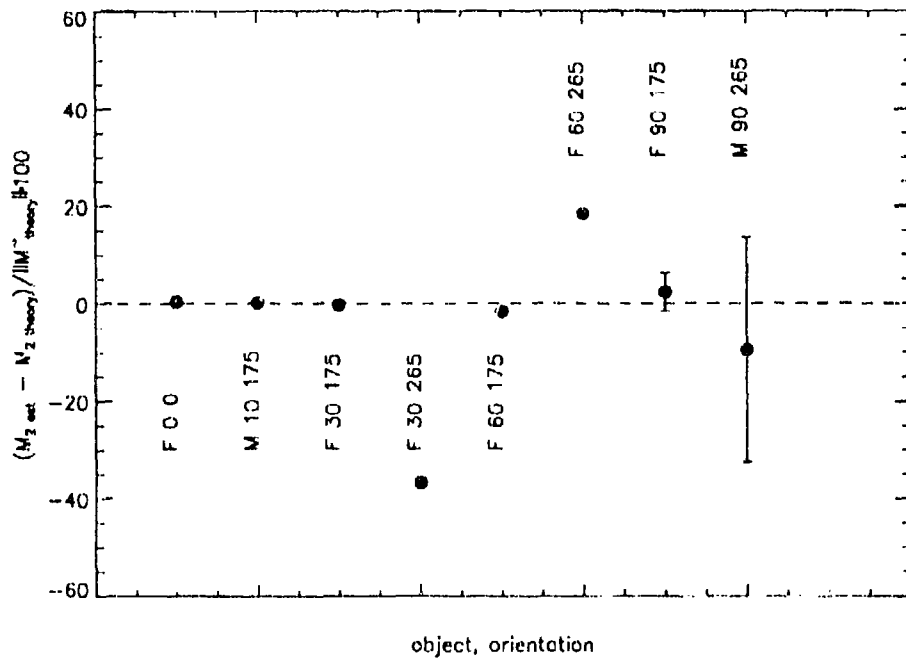
Figure 4.21

Difference between M_2 component estimate and theoretical M_2, as a percentage of the magnitude of theoretical $\vec{M}$ for two different objects and a number of different orientations. Points are labelled with a letter for object type and two numbers. The first gives the polar angle and the second gives the azimuthal angle in degrees. Points with error bars are unweighted averages of a number of estimates at different depths. Error bars are the standard deviations.
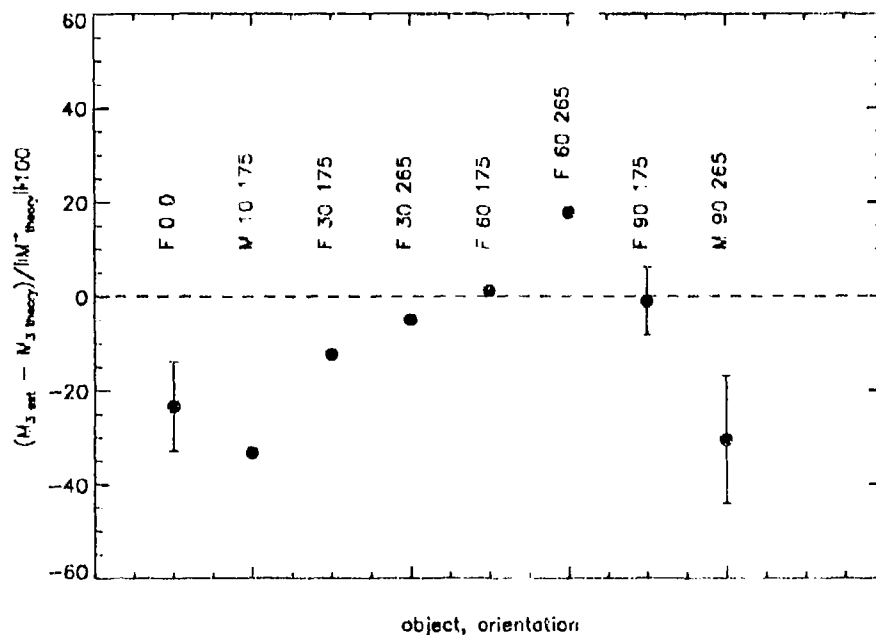
Figure 4.22

Difference between M_3 component estimate and theoretical M_3, as a percentage of the magnitude of theoretical $\vec{M}$ for two different objects and a number of different orientations. Points are labelled with a letter for object type and two number. The first gives the polar angle and the second gives the azimuthal ang; in degrees. Points with error bars are unweighted averages of a number of estimates at different depths. Error bars are the standard deviations.
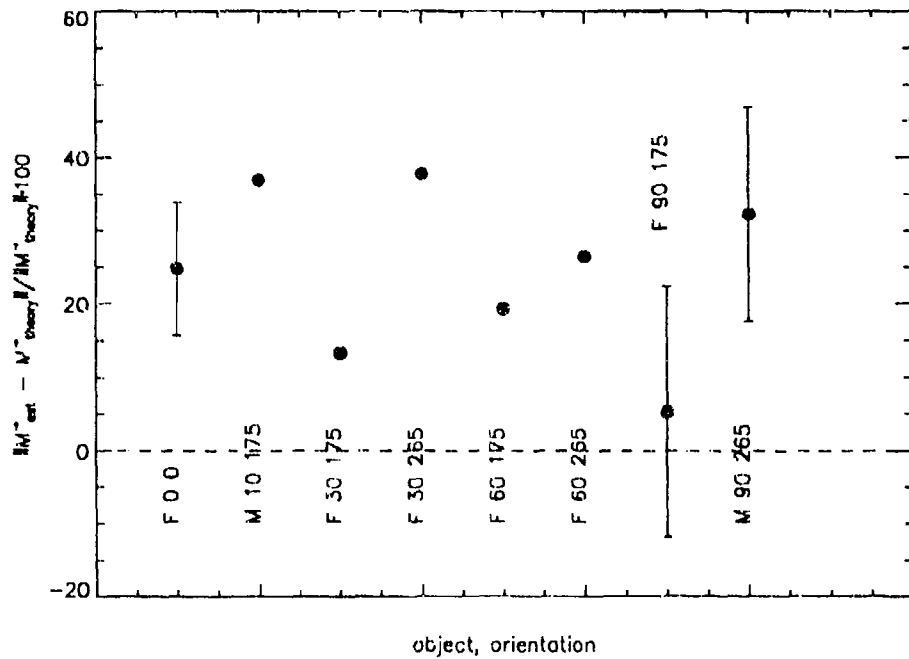
Figure 4.23

Magnitude of the vector difference between estimated $\vec{M}$ and theoretical $\vec{M}$, as a percentage of the magnitude of theoretical $\vec{M}$ for two different objects and a number of different orientations. Points are labelled with a letter for object type and two numbers. The first gives the polar angle and the second gives the azimuthal angle in degrees. Points with error bars are unweighted averages of a number of estimates at different depths. Error bars are the standard deviations.

5. Performance of Location Estimation

5.1 Sources of Error in Location Estimation

In the previous Chapter, we saw that the location algorithm produced estimates of both location and moment components that deviated from the measured or theoretical values by amounts that were on average significantly greater than the experimental precision (Figs. 4.20 to 4.23). In this Chapter we will analyse the sources of these deviations in an attempt to identify ways to minimize or eliminate them.

There are a number of possible sources of error in estimating the dipole location and moment of a compact object when using the algorithm of Section 2.2 with a total field magnetometer. These may be grouped in the following manner:

1. Experimental Errors and Uncertainties

   (a) Sensor Positional Uncertainty - Deviations of the sensor from its assumed position will introduce errors. The dominant error term is due to deviations of the sensor from a known plane. These have been quantified in [10]. To summarize briefly, the accuracy of dipole parameter estimates was found to be independent of the uncertainty in sensor position parallel to the plane, if the latter was $\leq 5\%$ of the depth. The percentage errors in both position and dipole moment component estimates were roughly equal to the percentage uncertainty (relative to the depth) in sensor position orthogonal to the plane, if the latter was $\leq 5\%$ of the depth.

   (b) Finite Volume of Magnetic Sensor Head - The algorithm assumes that a magnetic measurement is taken at an infinitesimal point in space, but the magnetic sensor head is a finite cylinder with a length of ~ 17 cm and a diameter of ~ 6 cm. The measurement point has been assumed to be the geometric center of the active volume. If the field gradient is small, the measured field will be an accurate representation of the true field at that point. If the gradient is large, the effective measurement point will be shifted from the geometric center by an amount which is a function of the field gradient. This would produce larger errors for objects and orientations whose magnetic field maps have larger field gradients. The effect of finite sensor head volume is to introduce a position

dependent positional uncertainty in all three directions. Properly quantifying the uncertainty would require extensive modelling of the operation of the sensor head in relation to the gradients of the magnetic fields of typical spheroids.

(c) Magnetic Field Measurement Uncertainty - According to [10], assumed zero mean additive Gaussian errors, the accuracy of dipole parameter estimates is independent of SNR of the magnetic field, if the SNR of the field maximum in the measurement plane is greater than about 25. The smallest maximum encountered in this study was ~ 100 nT. The quantization error for the magnetometer system is 1 nT, so that the estimates should be independent of SNR. In addition, the spheroid field in the plane can have a large gradient, which combined with positional uncertainty, will produce errors that are neither Gaussian nor zero mean. Although gradients of ~ 2 nT/mm for a map with a 1000 nT maximum field and ~ 0.3 nT/mm for a map with a 150 nT maximum field were typically encountered, these occurred far from the extrema. Gradients near the extrema are, as one would expect, small. (This is, in fact, a strength of the extremum location estimator). Thus, errors due to magnetic field measurement uncertainty are expected to be negligible.

2. Location Algorithm Approximations

(a) Locating the Maximum and Minimum of the Magnetic Field in the Measurement Plane - A method that was successful with theoretical purely dipolar magnetic data was to search a coarse grid (~ 25 cm spacing) to quickly approximate the maximum and minimum positions and then to search a fine grid search (~ 2.5 cm spacing) to accurately locate the extrema [10]. For this study, practical experimental limitations made it necessary to use only a single search over a fixed grid which was fine in the X_1 direction ($\sim 2 - 3$ cm spacing) but coarse in the X_2 direction ($\sim 5 - 10$ cm spacing). This may cause an error which is depth dependent, since the spatial extent of the field is a function of depth whereas the grid spacing is fixed. In addition, the position of the extrema are located by assuming that the centroid calculated in the vicinity of the extremum coincides with the extremum position. For skewed peaks, this will produce an error.

(b) Use of Total Magnetic Field Measurements - The algorithm is strictly speaking correct only for vertical component magnetic field measurements. Total magnetic field values approximate, but are not identical to, vertical component values in geographical regions with high magnetic inclinations, such as the location of our laboratory. This will cause a bias in the estimation of dipole parameters, but will not cause an increase in the standard deviation of the estimates.

(c) errors related to computer implementation. - These include approximations to inverse functions unique to the algorithm and are negligible compared to other sources of error.

3. Deviation of Field of a Compact Object From Pure Induced Dipole

(a) Higher Order Moments - Ferrous objects, when placed in a magnetic field, such as that of the earth, acquire induced magnetization whose magnitude and direction is a function of the primary field strength, ferromagnetic susceptibility of the body, its shape and its orientation with respect to the primary field. This produces a dipolar field that can be attributed to a dipole moment source located at the object center. However, for all objects except a sphere, there are also field components due to higher order moments. These field terms are generally smaller than and decrease with distance from the object faster than the dipole term. At close distance, the fields due to higher order moments will add a distortion term to the dipole field and lead to errors in dipole parameter estimation. For the algorithm used in this report, the effect of higher multipole fields is to shift the extrema positions and alter their magnitude. For spheroids similar in shape and size to artillery shells at close range in geometries similar to those of these experiments (depth 4 times the maximum dimension and 18 times the minimum dimension), the maximum octupole field varies from 3 to 8% of the maximum dipole field [8].

(b) Remnant Magnetization - Ferrous objects may also have remnant magnetization which is a function of the metallurgical properties of the object as well as its thermal, mechanical and geomagnetic history. Remnant magnetization is very difficult to model since its strength and direction are often unknown for an individual object and may vary from object to object of the same shape and size. Remnant magnetization will in general not be purely dipolar. The dipole component of the remnant magnetization will add vectorally to the induced moment, which may make it difficult to use the estimated total dipole moment to classify the object. Higher order multipoles will cause a distortion to the dipole field, just as those from the induced magnetization do, which will increase the error in estimating the source location and dipole moment. Fortunately, past evidence has suggested that remnant magnetization can be neglected for some applications, including ordnance detection [7]. Even when present in artillery shells, some evidence indicates that remnant magnetization is small and is similar for individual shells of the same type [8].

Of the non-negligible errors mentioned above, positional uncertainties will random in nature and will contribute to the precision of the estimates but not the accuracy (bias). The maximum uncertainties in position were roughly 1.4 cm for X_1 (determined mainly by the finite measurement time of the magnetometer), 1 cm in X_2 (dictated by swerving of the magnetometer cart) and 0.2 to 0.5 cm in X_3 (caused by fluctuations in flatness of the measurement table). Since the uncertainty in both X_1 and X_2 was < 5% of the depth for all depths, [10] implies that these uncertainties should have a negligible contribution to the overall precision. To compare the measured precision with the precision attributable to the positional uncertainty, we can average the component precision of the location and moment components of Tables VII and VIII to produce Table X. It is seen that the precision of estimated location components is in reasonable agreement with [10], that is, the average

precision in the components is roughly equal to the percentage uncertainty in X_3. The precision of the estimated moment components is slighly higher than the uncertainty in X_3 but is still in reasonable agreement with [10]. In any case, it is clear that a substantial fraction, if not the major portion, of the uncertainty (precision) in dipole location and moment vector estimates is due to positional uncertainty.

The bias in estimation in the dipole location and moment vector estimates must then be due to the remaining five non-negligible sources of error. We shall next study the error in estimation using magnetic field maps generated by computer using a mathematical model to resolve some of the remaining sources.

5.2   Location Estimates for Theoretical Total Field Data

If the location algorithm is applied to magnetic field data generated by the mathematical model of Section 2.4, errors due to positional and magnetic measurement uncertainties are eliminated. Also, the true magnetic dipole moment is available to compare with the estimated dipole moment, s'nce there is no remnant magnetization. It will then be possible to investigate bias in estimation due to finite volume of the sensor head, finding the field maximum and minimum in the plane, higher order moments and the use of total field measurements.

Examples of typical magnetic field maps obtained using the model are shown in Figures 5.1 to 5.4. These should be compared with Figures 4.1 to 4.4. The shapes and peak field values of the experimental and theoretical maps are very similar as one would expect given the similarity between theoretical and experimental dipole moments (Figs. 4.20 to 4.22).

The location estimation algorithm was applied to the same object types and orientations at depths similar to those that were used in the experimental measurements. The results are shown in Tables XI and XII. These should be compared with Tables V and VI. Also, in Figs. 4.11 to 4.19, estimated dipole moment components for magnetic total field maps generated by computer using the mathematical model are shown in comparison to those estimated from experimental field maps.

The rms error, averaged (unweighted) over all cases in Tables V, XI, VI and XII, and its standard deviation are used as a rough measure of estimation performance for purposes of comparison. From the tables, the average error in estimation of the location vector is 0.04 m ± 0.01 m for computer generated data versus 0.05 m ± 0.02 m for experimental data. The average error in estimation of the dipole moment vector is 22 % ± 6 % (expressed as a percentage of the moment magnitude) for computer generated data versus 27 % ± 10 % for experimental data. Estimation errors for both experimental and computer generated data are significantly larger than the average precision, which from Tables VII and VIII is 0.003 m ± 0.002 m for the location vector and 4.1 ± 3.0 % for the moment vector. The error in estimation of the location vector is largely independent of whether the data is experimental

x_{03} (m)	=	−0.598000
e	=	3.50000
a (m)	=	0.0525000
μ_{r1} / μ_{r2}	=	1000.00
θ (°)	=	0.00000
ψ (°)	=	0.00000
B_0 (nT)	=	60000.0
θ_0 (°)	=	17.0000
ϕ_0 (°)	=	180.000

Figure 5.1

Theoretical total magnetostatic field map versus position in a plane for spheroid F at $\theta = 0°$. Spheroid parameters are shown at right. Ambient (earth's) field magnitude has been subtracted.

Figure 5.2

Theoretical total magnetostatic field map versus p 'tion in a plane for spheroid F at $\theta = 30°$ and $\phi = 175°$. Spheroid parameters are shown at right. Ambient (earth's) field magnitude has been subtracted.

Figure 5.3

Theoretical total magnetostatic field map versus position in a plane for spheroid F at $\theta = 60°$ and $\phi = 175°$. Spheroid parameters are shown at right. Ambient (earth's) field magnitude has been subtracted.
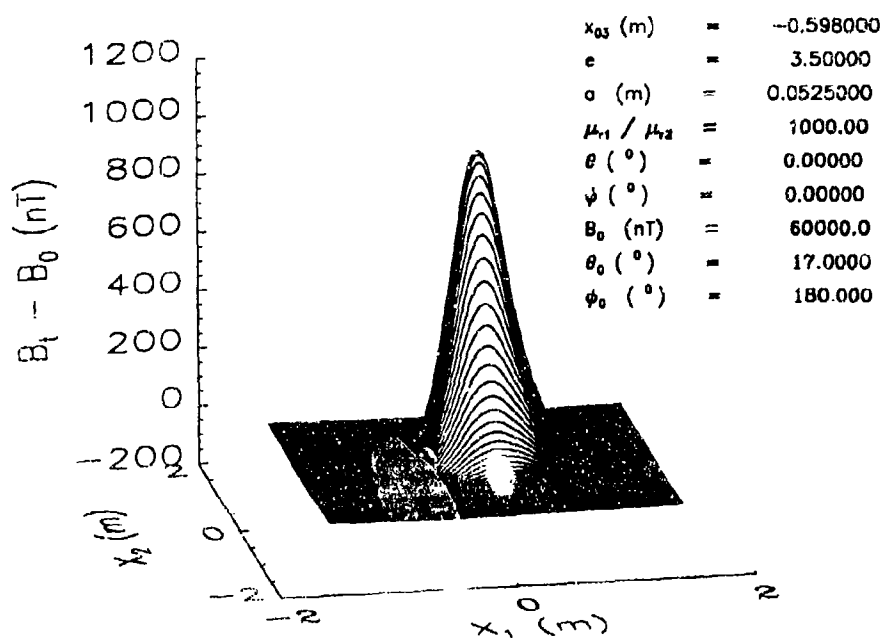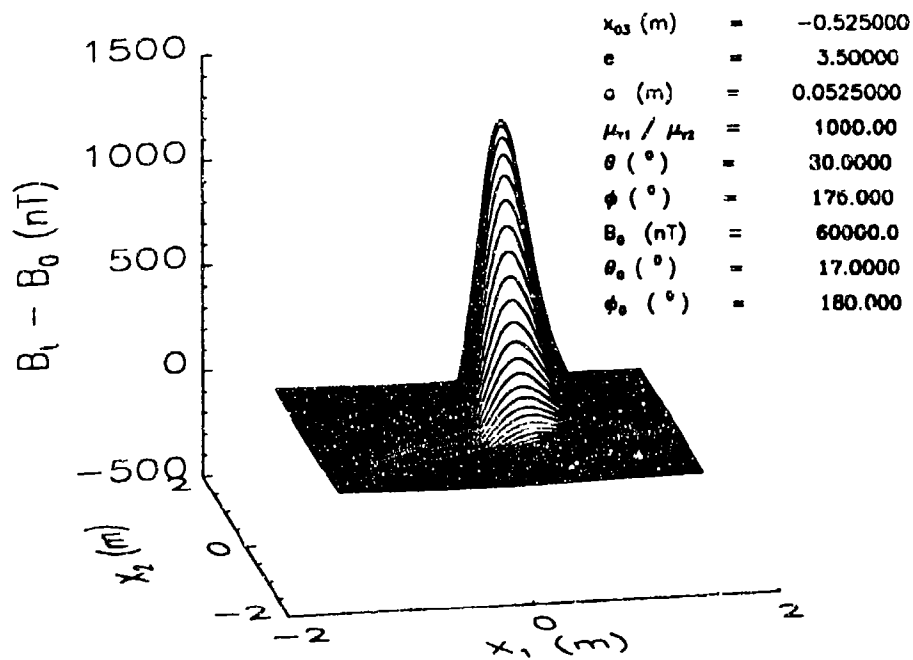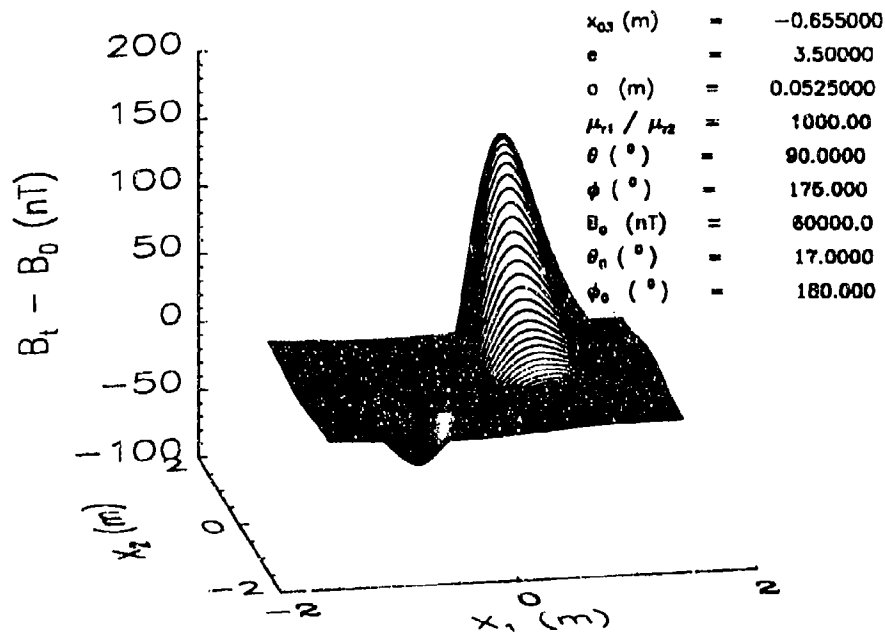
Figure 5.4

Theoretical total magnetostatic field map versus position in a plane for spheroid F at $\theta = 90°$ and $\phi = 175°$. Spheroid parameters are shown at right. Ambient (earth's) field magnitude has been subtracted.

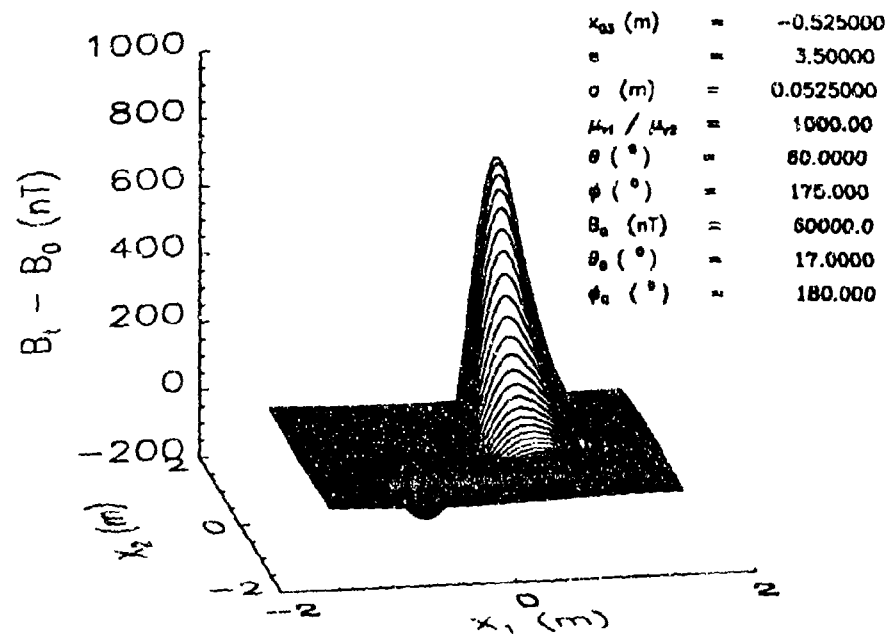or theoretical. Trends in overestimation or underestimation of the depth are similar to those discussed in Chapter 4 for the experimental data. Dipole moment estimation errors for computer generated data are slightly smaller than those for experimental data. This implies that the positional error in these experiments has little influence on location and moment vector estimation. This also suggests that remnant magnetization in the spheroids must be small compared to the induced magnetization, since the theoretical moments have been used for comparison to the estimates for both the theoretical and experimental magnetic maps.

To further investigate trends as a function of object shape, orientation and depth, the rms estimation error for vertical and horizontal type M and F spheroids were plotted for a number of depths. In addition, the rms estimation error for a spheroid that was neither vertical nor horizontal and a sphere were also plotted. These are shown in Figs. 5.5 and Figs. 5.6.

The figures reveal a number of points. The error in estimation of the location vectors is generally bigger than the precision in estimation (Fig. 4.5) for both computer generated and experimental data. Since the bias for both data sets is similar, this suggests that the finite volume of the magnetometer sensor head is not a significant source of error. (Because the field gradient decreases with distance from the source, the tight geometry of these experiments is probably a worst case for errors due to finite sensor volume.) Generally speaking, the error shows some variation with depth but it appears almost random. The error also appears to be independent of object shape. The error appears to depend slightly on the object orientation and the same orientation yields similar errors for different object shapes. Specifically, the 90 90 orientation yields the smallest error at low depths (< 0.7m) and the 10 0 orientation is smallest at greater depths. The 90 175 orientation yields the largest error for all depths. Since the error for the sphere is in the middle of the range of errors, higher order moments do not seem to have a large effect on the estimation of location. The variation of error with depth suggests that the main contributor to the error is estimation of the position of the field extrema and the use of total field in place of vertical component magnetic data, since both are dependent on depth for a fixed sampling grid. These two sources of error are further indicated because, as has been seen, both errors should show a dependence on the object orientation.

The spread of the moment estimation error curves is comparable to precision of moment estimates (Fig 4.6), but there is a clear bias in estimation for all curves. The error shows a small, seemingly random dependence on depth except for the F 90 175 error at depths ≤ 0.5 m which increases with decreasing depth. The error for the sphere is smaller than any other object or orientation except for F 90 175 at depths ≥ 0.6 m. This suggests that the presence of higher order multipole moments is significant in dipole moment estimation, but the effect is small compared to the overall bias for the error curves. Since the shapes of magnetic field maps are a function of object shape and orientation, it is not possible to separate the effects of higher order multipoles from the error in extrema position estimation. The important point for object classification is that the moment estimates for a given object and orientation vary by between 2 and 4% of the moment magnitude as the depth varies.

Figure 5.5

rms location vector estimation error for computer generated magnetic
total field maps for two spheroids at various orientations and a sphere.

Figure 5.6

rms moment vector estimation error for computer generated magnetic
total ..eld maps for two spheroids at various orientations and a sphere.

The bias is unimportant, since the estimated moments can be used in the design set. This suggests that the limiting misclassification error will be between roughly 1.4 and 2.4% [11] if the experimental error is substantially less than the algorithmic and approximation errors. For the present experimental precision (4.1 ± 3.0%), the misclassification error should be roughly between 2 and 5% (assuming quadrature error summation) if the design set were experimentally obtained.

For both the location and dipole moment estimation the F 90 175 curves do not follow the same trends as the others. The location error is higher than the other errors while the moment curve has a sharp depth dependency not seen in the other moment errors. The reason for this is not known.

It is initially tempting to think that one can estimate the remnant dipole moment by subtracting the dipole moments estimated for experimental maps from those estimated for theoretical maps with object type, orientation and depth fixed (Figs. 4.11 to 4.19). Averaging over depth would then give the remnant magnetization for a given object and orientation (which should be related to other orientations by a simple Euler rotation matrix). Unfortunately, as we have just seen, the bias in estimation varies with object orientation. This is presumably due to the differing shapes of the magnetic maps which have different errors when estimating the extrema positions. This variation is small but is clearly of the same order of magnitude as the deviation between experimental and theoretical estimates. A simple subtraction of experimental and theoretical moment estimates would not take into account the difference in bias due to the differing moments of the experimental and theoretical data. There may be ways to more precisely estimate the contribution of remnant magnetization to the total dipole moment. For example, one might use theoretical moments to derive the error bias as a function of moment component estimates. This could, in turn, be applied as a correction to the experimental estimates. Then, one could subtract the theoretical dipole moments from the corrected experimental estimates. It is hoped that this can be investigated in the future.

5.3 Location Estimates for Theoretical Vertical Component Field Data

From the previous section, it was seen that, if we exclude experimental errors (positional uncertainty and remnant magnetization), there are three other possible sources of error that can contribute significantly to the estimation error. Th se are the estimation of extrema positions, the use of total field magnetic data and the presence of higher order moments. To eliminate the effect of using the total magnetic field of the spheroid as an approximation to the vertical component of the magnetic field, the location algorithm was applied to magnetic field maps of the vertical magnetic component (B_3). The rms estimation error was calculated for the same objects, orientations and depths as in Figs. 5.5 and 5.6. These are shown in Figs. 5.7 and Figs. 5.8.

The error in estimation of the location vector is generally slightly smaller for a given case than when total field data are used. Other trends are very similar to the total field data.
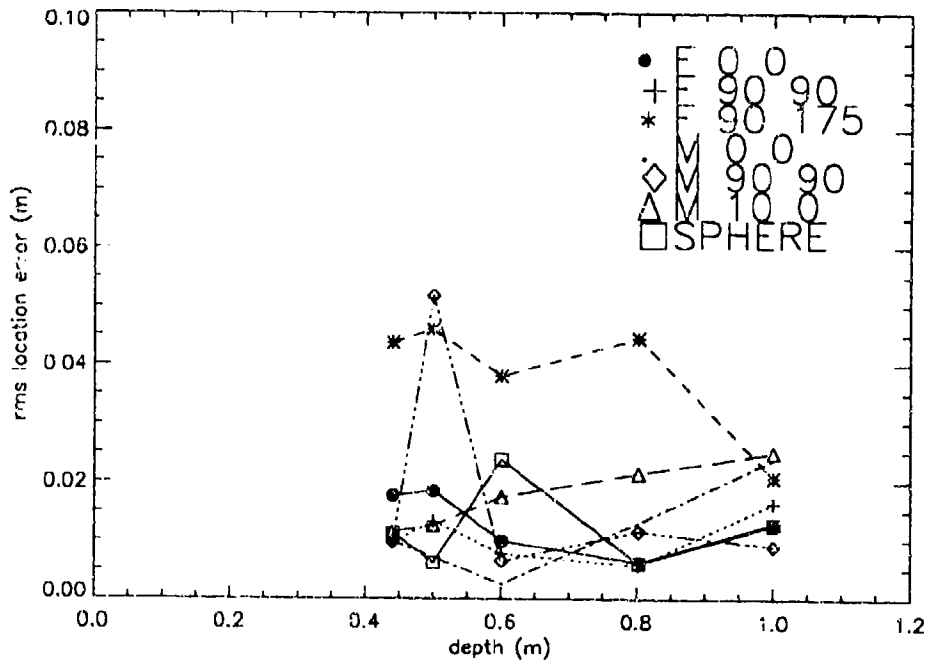
Figure 5.7

rms location vector estimation error for computer generated magnetic
vertical component field maps for two spheroids at various orientations
and a sphere.
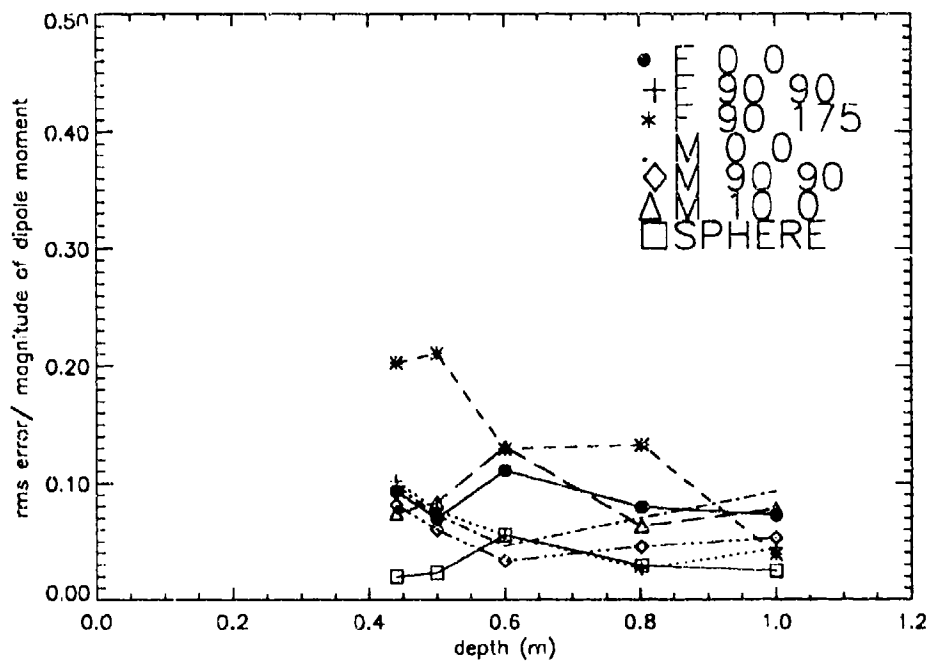
Figure 5.8
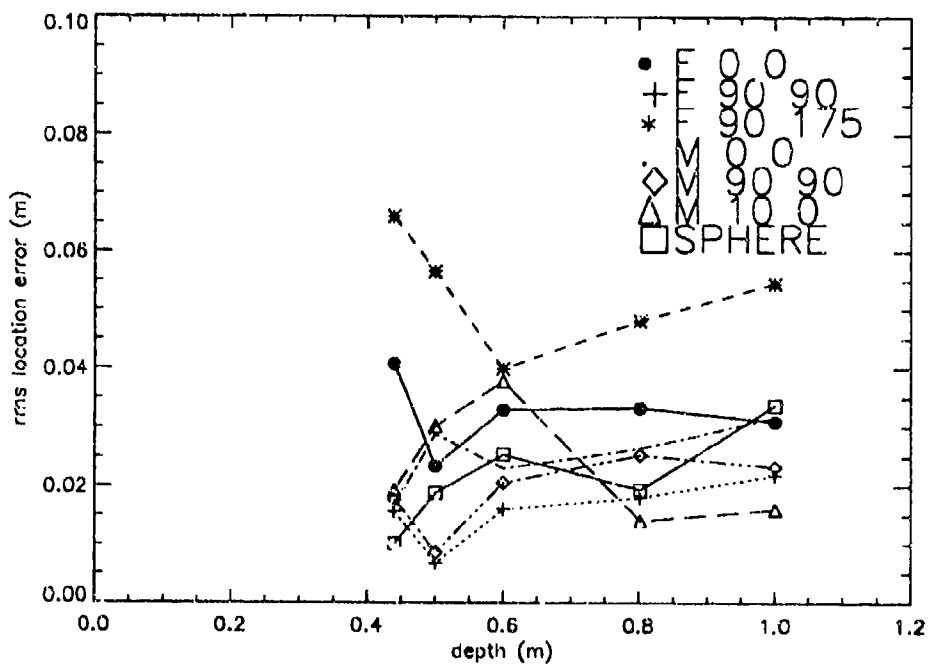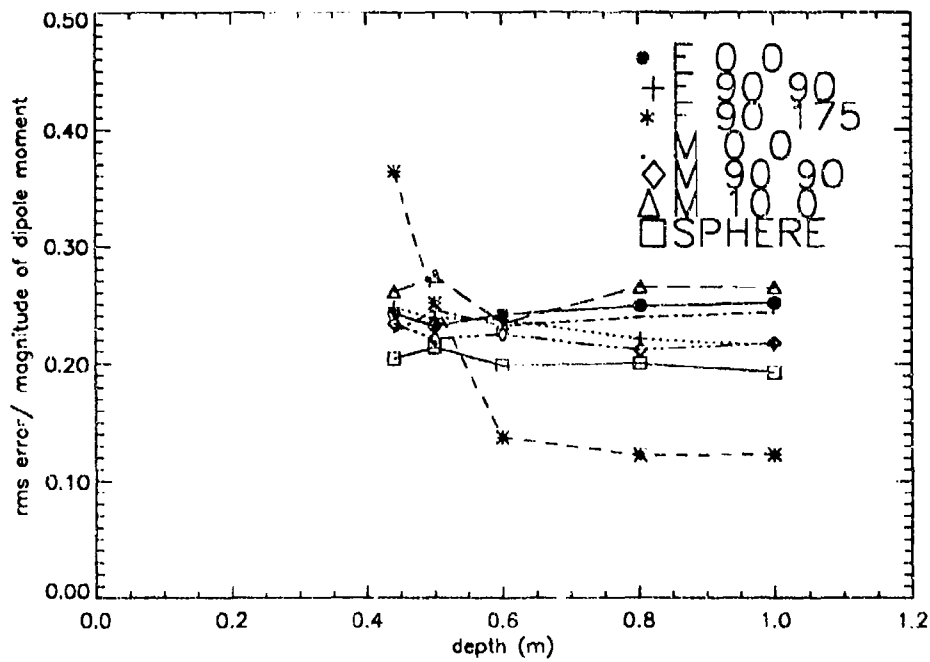
rms moment vecto estimation error for computer generated magnetic
vertical component field maps for two spheroids at various orientations
and a sphere.

Again the depth dependency is small and almost random in nature. The error for the sphere is, as before, not the lowest for all cases. The 90 175 case again yields the highest error at all depths, except for M 90 90 at 0.5 m. It is not clear why the error for this latter case is anomalously high.

The spread in moment estimation error for vertical component data is similar to that of the total field data, but the bias for the former is significantly less. This suggests that the use of total field data introduces a bias in estimation for ɔ dipole moment. As for the total field data, the error for vertical component data is roughly constant with depth for a given object and orientation. The error in estimation of the sphere is significantly less than all other cases except M 90 90 and M 0 0 at 0.6 m depth, which indictates that higher order moments still contribute somewhat to the error. To crudely estimate the contribution of the various sources of error, we note that the bias in estimation of the sphere for vertical component data is roughly 2 to 6% of the moment magnitude, whereas for total field data it is 20%. This suggests that the error due to the total field approximation varies from 14 to 18% of the moment magnitude. Error due to estimation of extrema positions and higher order moments then varies from 0 to 8% of the moment magnitude which is in rough agreement with that for the total field data. This seems reasonable, since in Section 5.1 it was noted the maximum octupole field varies from 3 to 8% of the maximum dipole field for spheroids in geometries similar to ours.

Depth (m)	Range of Uncertainty in X_3 (% of Depth)	Average Location Component Precision (% of Depth)	Average Moment Component Precision (% of Moment Magnitude)
0.390	0.5 - 1.3	2.0	4.7
0.438	0.4 - 1.1	1.0	2.5
0.500	0.4 - 1.0	1.9	-
0.525	0.4 - 1.0	3.9	-
0.565	0.4 - 0.9	0.2	0.3
0.598	0.3 - 0.8	0.8	2.4
0.698	0.3 - 0.7	0.2	0.7
0.802	0.2 - 0.6	0.5	1.8

Table X

Comparison of uncertainty in X_3 measurement with precision of estimated location and dipole moment vector components. Precision of location (moment) components is the average of the precision of the 3 location (moment) components for a given depth, taken from Tables VII and VIII.

Spheroid Type, Orientation	Measured			Estimated		
	X_{01} (m)	X_{02} (m)	X_{03} (m)	X_{01} (m)	X_{02} (m)	X_{03} (m)
F 0 0	0.000	0.000	0.440	-0.004	0.000	0.399
	0.000	0.000	0.500	-0.015	0.000	0.477
	0.000	0.000	0.600	-0.007	0.000	0.568
	0.000	0.000	0.802	-0.014	0.000	0.772
	0.000	0.000	1.000	-0.022	0.000	0.978
F 90 175	0.000	0.000	0.440	-0.028	0.004	0.500
	0.000	0.000	0.500	-0.031	0.010	0.546
	0.000	0.000	0.525	-0.037	0.010	0.546
	0.000	0.000	0.600	-0.037	-0.003	0.579
	0.000	0.000	0.655	-0.031	0.004	0.673
	0.000	0.000	0.802	-0.045	0.003	0.818
	0.000	0.000	1.000	-0.051	0.003	1.018
M 90 265	0.000	0.000	0.440	-0.015	0.000	0.450
	0.000	0.000	0.500	-0.009	0.000	0.500
	0.000	0.000	0.600	-0.011	0.000	0.583
	0.000	0.000	0.802	-0.022	0.000	0.789
	0.000	0.000	1.000	-0.019	0.000	0.987
M 10 175	0.000	0.000	0.500	0.010	0.000	0.472
F 60 175	0.000	0.000	0.525	-0.041	0.004	0.546
F 30 175	0.000	0.000	0.525	-0.041	-0.003	0.521
F 60 265	0.000	0.000	0.525	-0.040	-0.021	0.553
F 30 265	0.000	0.000	0.525	-0.018	-0.031	0.504

Table XI

Location vector estimation results using magnetic field data generated from the computer model of Section 2.4.

spheroid type, orientation	depth (m)	Theoretical			Estimated		
		M_1 (A·m²)	M_2 (A·m²)	M_3 (A·m²)	M_1 (A·m²)	M_2 (A·m²)	M_3 (A·m²)
F 0 0	0.440	0.0649	0.0000	1.0685	0.2685	0.0000	0.9073
	0.500	0.0649	0.0000	1.0685	0.3072	0.0000	1.0144
	0.600	0.0649	0.0000	1.0685	0.2965	0.0000	0.9535
	0.802	0.0649	0.0000	1.0685	0.3081	0.0000	0.9593
	1.000	0.0649	0.0000	1.0685	0.3219	0.0000	0.9881
F 90 175	0.440	0.3247	-0.0227	0.2123	0.4640	-0.0361	0.2326
	0.500	0.3247	-0.0227	0.2123	0.4214	-0.0360	0.2137
	0.525	0.3247	-0.0227	0.2123	0.4362	-0.0470	0.2208
	0.600	0.3247	-0.0227	0.2123	0.3707	-0.0306	0.1864
	0.655	0.3247	-0.0227	0.2123	0.3614	-0.0280	0.1828
	0.802	0.3247	-0.0227	0.2123	0.3600	-0.0162	0.1812
	1.000	0.3247	-0.0227	0.2123	0.3615	-0.0231	0.1820
M 90 265	0.440	0.0579	0.0000	0.1893	0.1033	0.0000	0.1802
	0.500	0.0579	0.0000	0.1893	0.0963	0.0000	0.1685
	0.600	0.0579	0.0000	0.1893	0.0889	0.0000	0.1575
	0.802	0.0579	0.0000	0.1893	0.0923	0.0000	0.1655
	1.000	0.0579	0.0000	0.1893	0.0949	0.0000	0.1674
M 10 175	0.500	0.1045	-0.0041	0.4548	0.1106	0.0000	0.3585
F 60 175	0.525	0.6291	-0.0494	0.5393	0.7586	-0.0649	0.5364
F 30 175	0.525	0.4992	-0.0380	0.9674	0.6788	-0.0199	0.9528
F 60 265	0.525	0.0987	0.3864	0.4363	0.1423	0.4281	0.4861
F 30 265	0.525	0.0977	0.3750	0.8644	0.2140	0.2951	0.8032

Table XII

Dipole moment vector estimation results using magnetic field data generated from the computer model of Section 2.4.

6. Performance of Pattern Classification

Identification of objects from the estimated dipole moments was achieved using the continuous parameter pattern (CP) classifier of Section 2.3. Following [11], the design set for each object consisted of a dipole moment for each 15° increment in θ and ϕ, $0 \le \theta \le 90°$, $0 \le \phi \le 360°$.

T.. design set for one object requires 225 dipole moment vectors. At 8 - 15 minutes per dipole moment measurement for the present instrument, a design set using moments estimated from experimental data would require approximately 30 to 55 measurement hours per object. Since about 8 to 10 objects are needed to reasonably represent the range of typical unexploded ordnance that is available, between 240 and 550 hours of measurement time would be required in total. On the other hand, a dipole moment design set derived from Equation 2.33 of the model of Section 2.4 could be obtained in a few minutes. Since our aim was to test the proof of concept of real-time location and identification of objects, in the interests of expediency we chose to use the theoretical design set. In doing so, it was recognized that a systematic difference between estimated and theoretical dipole moments, as we have seen in the previous Section, would increase the misclassification error rate over what would be achieved with an experimentally derived design set.

The design set used in the classification is shown in Table XIII.

Results of the classification using the experimentally estimated moments are given in Table XIV for spheroid F and in Table XV for spheroid M. For each case, the classification algorithm provided a ranked list of all classes and the closest distance from each class to the test vector. Here, only the highest ranked (most likely class) has been show n for each case.

Spheroid F was quite successfully classified with a misclassification rate of 3/29 (10.3%). The orientation angles of the spheroid were also estimated quite well. For θ, all estimates for correctly classified cases were within 10° of the true angle and roughly 46% were within 5°. For ϕ, all estimates for correctly classified cases were within 15° of the true angle, roughly 92% were within 10° and 69% were within 5°.

At first glance, results were less encouraging for Spheroid M. None of the cases were classified correctly. However, the spheroid was consistently classified as class number 3. All estimates of θ for the 90 265 orientation were within 21° of each other and 5/6 were within 5° of each other. 4/6 estimates of ϕ for the 90 265 orientation, all at the same depth,

were within 5° of each other. The remaining 2/6 were not even close to one another or the others.

Further light can be shed on the classification error by examining the individual misclassifications in Table XVI. Here we have listed classification results for each case ranked in descending order down to and including those for the true object. The distance measure presented in column 7 is d_i^2 (Equation 2.16).

Of the misclassifications of object 6, the correct object is ranked second 4/7 times. The estimates of angles have a larger spread for object 3 than for the correct classifications of object 4. This suggests that, although object 3 is chosen as the most likely class when experimental data for object 6 is presented, the computer generated dipole moments of object 3 are not as good an approximation to the experimental moments of object 6 as computer generated moments of object 4 are to experimental moments of object 4. The consistency with which object 6 is classified as object 3 can be explained by noting that class 3 and class 6 objects are the closest in shape of the objects in the design set. A class 3 spheroid has a length of 22.5 cm and a width of 9 cm, while a class 6 spheroid has a length of 23.6 cm and a width of 11.8 cm. A small amount of remnant magnetization together with the previously described errors in estimating the dipole moment, can easily account for the misclassification.

Object 4 is misclassified 3 times as a sphere. In addition, object 6 is ranked ahead of it in all 3 cases. Since object 4 is classified correctly the remainder of the time, these misclassifications are likely a reflection of the error in estimating the dipole moment in the depth range between 0.5 and 0.6 m. That range exhibits the largest deviation between experimental and computer generated moments for Spheroid F at 0 0 (Figs. 4.11 to 4.13).

The consistency or repeatability of classification is really more important than the correct choice of object, since if object "a" is always classified as object "b", one can merely switch the assignments upon completing the classification. (This assumes, of course, that object "b" is always classified as something else!) If we thus consider the experimental dipole moments for Spheroid M to be most closely represented by the computer generated moments of the class 3 spheroid, the misclassification rate is 3/36 (8.3%).

Finally, if we consider only the two objects for which experimental measurements were made, we see that only 4/36 cases (11.1%) were classified incorrectly.

Overall, the misclassification rate is encouraging but improvement is desirable. The misclassification rate of the pattern classifier is integrally linked to the error in estimation of the dipole moment by the location algorithm. There are a number of things that can be done to improve the misclassification rate. One obvious solution is to use a design set based on estimated dipole moments from experimental data. Although this would be time consuming using the instrument of this investigation, such a design set will be obtained. Further, a new multisensor fluxgate gradiometer, which we are presently developing, will allow location and dipole moment estimation without moving the sensor. If successful, this should speed up design set acquisition by at least a factor of five. Better extrema estimation will improve the misclassification rate. This might be achieved by locating the true peaks in the field map

as opposed to locating the centroid. One way to do this is to regularize the sampling grid, so that two dimensional interpolation routines can be used to more accurately pinpoint the extrema. If depth dependence in the error bias cannot be eliminated, design sets could be stored for various depths to minimize the depth dependent estimation bias. Problems with this approach include the need for substantial amounts of microprocessor memory and the time to collect a very large design set. A model for bias as a function of estimated moment component may be developed. This could then be applied as a correction to the estimated moments prior to classification. These items will be the subject of later investigations.

Class Number	Label	a (m)	e	Type of Unexploded Ordnance Resembled
0		0.01	3.75	20mm shell
1		0.02	3.4	40mm shell
2		0.03	2.5	60mm shell
3		0.045	2.5	81mm shell
4	Spheroid F	0.0525	3.5	105mm shell
5		0.09	3.5	155mm shell
6	Spheroid M	0.05896	2.0	
7		0.10	1.0	sphere

Table XIII

Objects used in design set for classification studies. Spheroid parameters are defined in Section 2.4. Labels refer to the objects for which exper-mental data is available. Last column shows the unexploded ordnance type that the spheroid is intended to loosely represent.

Class Number	θ (°)	ϕ (°)	depth (m)	Closest Class Number	Estimated θ (°)	Estimated ϕ (°)
4	0	-	0.802	4	5.05	193.08
4	0	-	0.802	4	6.83	192.27
4	0	-	0.802	4	8.35	193.35
4	0	-	0.698	4	7.20	189.43
4	0	-	0.698	4	6.99	207.65
4	0	-	0.598	4	6.49	192.72
4	0	-	0.598	4	7.53	190.53
4	0	-	0.598	4	7.37	193.12
4	0	-	0.598	4	6.87	191.14
4	0	-	0.598	4	8.90	173.51
4	0	-	0.598	4	10.31	178.30
4	0	-	0.598	4	5.91	221.92
4	0	-	0.565	7	0.00	15.00
4	0	-	0.565	7	0.00	15.00
4	0	-	0.50	7	15.00	0.00
4	90	175	0.655	4	84.18	0.00
4	90	175	0.525	4	85.80	174.17
4	90	175	0.44	4	89.29	0.71
4	90	175	0.39	4	85.25	12.59
4	90	175	0.39	4	87.82	6.13
4	90	175	0.39	4	86.52	4.01
4	90	175	0.39	4	85.79	0.00
4	90	175	0.39	4	89.32	169.79
4	90	175	0.39	4	84.89	0.00
4	90	175	0.39	4	85.98	0.00
4	60	175	0.525	4	59.61	176.44
4	30	175	0.525	4	39.37	175.46
4	60	265	0.525	4	52.62	259.39
4	30	265	0.525	4	32.13	256.86

Table XIV

Results of classifying dipole moments of spheroid F estimated from experimental magnetic field maps using the CP classifer and the design set of Table XIII.

Class Number	θ (°)	ϕ (°)	depth (m)	Closest Class Number	Estimated θ (°)	Estimated ϕ (°)
6	90	265	0.58	3	70.36	19.13
6	90	265	0.468	3	86.43	254.58
6	90	265	0.438	3	68.56	126.30
6	90	265	0.438	3	70.60	124.40
6	90	265	0.438	3	71.40	123.59
6	90	265	0.438	3	67.64	127.36
6	10	175	0.50	3	3.09	29.08

Table XV

Results of classifying dipole moments of spheroid M estimated from experimental magnetic field maps using the CP classifer and the design set of Table XIII.

True Class Number	θ (°)	ϕ (°)	Depth (m)	Rank	Class Number	Minimum Squared Distance to Class (Relative Units)	Estimated θ (°)	Estimated ϕ (°)
6	90	265	0.58	0	3	2.840e-04	70.4	19.1
				1	2	7.869e-04	15.0	173.7
				2	1	4.741e-03	15.0	180.0
				3	6	5.209e-03	75.0	35.4
6	90	265	0.468	0	3	1.189e-07	86.4	254.6
				1	2	5.168e-04	28.0	219.6
				2	1	3.682e-03	20.1	210.0
				3	6	7.717e-03	90.0	75.0
6	90	265	0.438	0	3	7.210e-04	68.6	126.3
				1	6	1.397e-03	86.7	120.0
6	90	265	0.438	0	3	7.118e-04	70.6	124.4
				1	6	1.819e-03	90.0	305.8
6	90	265	0.438	0	3	6.325e-04	71.4	123.6
				1	6	2.134e-03	90.0	304.0
6	90	265	0.438	0	3	8.752e-04	67.6	127.4
				1	6	1.057e-03	90.0	312.7
6	10	175	0.50	0	3	2.679e-04	3.1	29.1
				1	4	2.864e-03	68.4	2.2
				2	6	3.872e-03	41.0	4.9
4	0	-	0.50	0	7	3.131e-02	15.0	0.0
				1	6	7.072e-02	4.9	180.0
				2	4	8.203e-02	22.1	6.9
4	0	-	0.565	0	7	1.705e-02	0.0	15.0
				1	6	6.400e-02	15.0	180.0
				2	4	1.316e-01	7.4	26.7
4	0		0.565	0	7	1.632e-02	0.0	15.0
				1	6	6.182e-02	15.0	180.0
				2	4	1.314e-01	7.8	25.7

Table XVI

Individual cases of misclassification.

7. Conclusions

An improved "smart" microprocessor controlled magnetometer which can accurately locate and identify compact ferrous objects in real-time has been described. The instrument, which is person-portable, consists of a cesium vapour magnetometer mounted on a cart with a wheel-mounted optical encoder, a microcontroller, interface and a laptop computer. The instrument guides the operator in the collection of simultaneous magnetic field and position data in a horizontal plane above an object. Location is estimated by applying a custom-made noniterative location estimation algorithm to the data. A byproduct of the location algorithm is an estimate of the dipole moment which is used by a continuous parameter pattern classifier to identify the object. With the present instrument, 6 to 13 minutes are required to collect the data, location and dipole moment estimation requires 5 seconds and classification requires 30 seconds.

Detailed experiments were performed using two different ferrous spheroids, similar in shape to unexploded ordnance, in order to determine limits of error in estimation of the location and the dipole moment and the error in classification.

The precision in estimating location varied from 0.12 to 1.35% of the depth for a fixed object and orientation at a given depth. There was a slight variation in location estimate with object type and/or orientation which increased the location uncertainty to 1.67 to 1.90% of the depth. The precision in estimating the dipole moment varied from 0.51 to 8.21 % of the dipole moment magnitude. There was a slight increase in uncertainty as depth decreased, but the precision was not closely correlated with peak magnetic field.

All three components of the location estimate had a depth dependent bias which was larger than can be accounted for by the precision of the estimation. The X_{01} component of the location was almost always overestimated. The X_{02} component was generally overestimated for depths less than 0.55 m and underestimated for depths between 0.55 m and 0.8m. A similar trend appeared to occur for the X_{03} component except that the crossover from overestimation to underestimation occured at about 0.45 m depth. Errors in X_{03} were generally larger than those for X_{01} and X_{02}, the root mean square (rms) error over all depths being 0.020 m for X_{01}, 0.019 m for X_{02} and 0.045 m for X_{03}. By comparison, the average precision for a fixed object and orientation was 0.005 m for X_{01}, 0.003 m for X_{02}, and 0.004 m for X_{03}.

There was a deviation between theoretical values and experimental estimates of the

dipole moment that was greater than the uncertainties in the estimates. The unweighted average difference between estimated and theoretical dipole moment components as a percentage of the theoretical dipole moment was $4.8 \pm 7.6\%$ for M_1, $-3.3 \pm 15.5\%$ for M_2, $-10.8 \pm 17.5\%$ for M_3 and $24.5 \pm 11.4\%$ for the magnitude of the vector difference. There was no clear trend with object type, orientation or depth.

Following quantification of the error in the estimation of location and dipole moment, sources of error and their relative effects were analysed. It was argued that a substantial fraction of the uncertainty (precision) in dipole location and moment vector estimates was due to positional uncertainty in the experiments.

By applying the location algorithm to magnetic total field data generated by computer using a mathematical model based on magnetization induced in spheroids by a uniform magnetostatic field, the effects of remnant magnetization and positional uncertainty could be eliminated. It was shown that the estimation error of the location vector was roughly independent of whether the magnetic field data was experimental or computer generated. Dipole moment estimation errors for computer generated data were slightly smaller than those for experimental data. This suggested that positional error in these experiments had little influence on location and moment vector estimation and that remnant magnetization in the spheroids must be small compared to the induced magnetization. It was shown that the finite volume of the sensor head was not a significant source of error for the geometry of these experiments. A variation of error with depth and object orientation was noticed for the computer generated data. This suggested that the main contributor to the error was estimation of the position of the field extrema and the use of total field in place of vertical component magnetic data.

The location algorithm was applied to magnetic vertical component field data generated from the computer model in order to determine how much of the error in estimation was due to using total field measurements to approximate the vertical component of the magnetic field. Since the bias in estimation of the sphere for vertical component data was roughly 2 to 6% of the moment magnitude, whereas for total field data it was 20%, this suggested that the error due to the total field approximation varied from 14 to 18% of the moment magnitude. It was estimated that the error due to estimation of extrema positions and higher order moments varied from 0 to 8% of the moment magnitude.

The analysis of error in the computer generated total magnetic field data allowed limits to be set on the misclassification rate that can ultimately be attained. The moment estimates for a given object and orientation were found to vary by between 2 and 4% of the moment magnitude as the depth varied. If the estimated moments were used in the design set, this suggests that the limiting misclassification error would be between roughly 1.4 and 2.4% if the experimental (mainly positional) error were substantially less than the algorithmic and approximation errors. For the present experimental precision ($4.1 \pm 3.0\%$), the misclassification error should be roughly between 2 and 5% (assuming quadrature error summation) if the design set were experimentally obtained.

Pattern classification was performed with a computer generated dipole moment design

set consisting of 8 objects including the 2 used in these experiments. The gross misclassification rate was 10.3% for the class number 4 spheroid and 100% for class number 6. Closer examination revealed that class 6 was always classified as class number 3, which is a similarly shaped spheroid. This is likely due to the deviation between the moment estimates for the experimental spheroid and the computer model. The repeatability of classification, that is, the percentage of cases in which an object is classified as the same class, is a better measure of classifier performance. The repeatability of classification was 91.7%. If we consider only the two objects for which experimental measurements were made, we see that only 4/36 cases (11.1%) were classified incorrectly.

The overall performance of the smart magnetometer is very encouraging, but additional studies need to be performed. Although remnant magnetization has been shown to be small in these and previous experiments, this must be verified by estimating moments for sets of identically shaped spheroids at fixed depths. This should also be repeated for unexploded ordnance. The possibility of accurately determining the relative contributions of remnant and induced magnetization should be investigated. A major source of error is the estimation of position of the magnetic field extrema. A possible improvement is to regularize the sampling grid for the magnetic field measurements so that two dimensional interpolation may be used to estimate the extremum position, rather than its centroid as is currently done. This appproach, which will be investigated, may improve the accuracy of the peak position estimates. The possibility of applying corrections to the total field data to improve its approximation to vertical component data should be investigated. One possible method to achieve this might be to use a three sensor orthogonal axis fluxgate total field magnetometer which is either on a stabilized platform or whose orientation angles with respect to a fixed coordinate system are known. Whether such a system is practical must be investigated. Most importantly, a comprehensive design set must be assembled from measured experimental magnetic field maps of objects of interest.

The last proposed study will require considerable time, given that between 6 and 13 minutes are required to collect the data for one dipole moment estimation. This laboratory, in conjunction with Pylon Electronics Ltd. of Ottawa, Canada, is presently developing a multisensor fluxgate gradiometer which will incorporate a modified Wynn-Frahm location algorithm [16] and the present pattern classifier. The gradiometer will be able to estimate location from a single measurement in space and hence sufficient data for a moment estimation will be collected in less than a second. To use a design set from the gradiometer in the magnetometer, the estimated dipole moments from one instrument must be nearly equal to those from the other. A comparative study of the dipole moment estimation errors for both the smart magnetometer and gradiometer will be conducted using the spheroid model, and later using real magnetic field and field gradient data.

DRES-SR-582

8. References

[1] R.Robertson. UNDEX site survey report (U). Report TR-303, Naval Explosive Ordnance Disposal Technical Center, Indian Head, MD, USA, September 1991. UNCLASSIFIED.

[2] J.E.McFee and Y.Das. Determination of the parameters of a dipole by measurement of its magnetic field. *IEEE Transactions on Antennae and Propagation*, AP-29:282–287, March 1981.

[3] J.M.Stanley and M.K.Cattach. An image processing magnetometer system for explosive ordnance detection. Report, Geophysical Research Institute, University of New England, Armisdale, NSW, Australia, 1989.

[4] Institut Dr. Forster. FEREX CAST 4.021.06 computer aided search technique to locate ferrous-metal objects. Sales Brochure, 1991. Prufgeratebau GmbH, Unternehmensbereich, Spezialprodukte, Postfach 15 64, D-7410, Reutlingen, Germany.

[5] Aprotec Ltd. CAMAD. Sales Brochure, circa. 1986. Enterprise House, Manchester Science Park, Lloyd Street North, Manchester, M15 4EN, England.

[6] J.E.McFee, Y.Das, and R.Ellingson. Locating and identifying compact ferrous objects. *IEEE Transactions on GeoScience and Remote Sensing*, GE-28(2):182–193, March 1990.

[7] J.E.McFee, M.Bell, B.Dempsey, R.Chesney, and Y.Das. A magnetostatic signature measurement and analysis system. *Journal of Physics E*, 18:54–60, January 1985.

[8] J.E.McFee and Y.Das. A multipole expansion model for compact ferrous object detection. In *Proceedings of the ANTEM Symposium on Antenna Technology and Applied Electromagnetics*, pages 633–638, University of Manitoba, Winnipeg, MN, Canada, August 1990.

[9] J.E.McFee. Electromagnetic remote sensing - low frequency electromagnetics (U). Special Report SSP-124, Defence Research Establishment Suffield, January 1989. UNCLASSIFIED.

[10] J.E.McFee and Y.Das. Fast nonrecursive method for estimating location and dipole
      moment components of a magnetic dipole. *IEEE Transactions on GeoScience and
      Remote Sensing*, GE-24:663–673, September 1986.

[11] J.E.McFee and Y.Das. A classifier for feature vectors whose prototypes are a function
      of multiple continuous parameters. *IEEE Transactions on Pattern Recognition and
      Machine Intelligence*, PAMI-10:599–606, July 1988.

[12] J.Stratton. *Electromagnetic theory*. McGraw-Hill, New York, 1941.

[13] Scintrex Limited, Concord, Ontario, Canada. *V101 Portable cesium high-sensitivity
      gradiometer system*.

[14] Motorola, Motorola Literature Distribution, Phoenix, AZ. *MC68332 user's manual*,
      MC68332UM/AD edition, 1990.

[15] J.T.Tou and R.C.Gonzalez. *Pattern recognition principles*. Addison-Wesley, Reading
      Massachusetts, 1974.

[16] W.Wynn, C.Frahm, P.Carroll, R.Clark, J.Wellhoner, and M.Wynn. Advanced super-
      conducting gradiometer/magnetometer arrays and a novel signal processing technique.
      IEEE Transactions on Magnetics, MAG-11:701–707, 1975.